Simulation of internal and external sulfate attacks of concrete with a generic reactive transport-poromechanical model

Adrien Socié, Frédéric Dubois, Yann Monerie, Mejdi Neji, Frédéric Péralès

To cite this version:

Adrien Socié, Frédéric Dubois, Yann Monerie, Mejdi Neji, Frédéric Péralès. Simulation of internal and external sulfate attacks of concrete with a generic reactive transport-poromechanical model. European Journal of Environmental and Civil Engineering, 2023, 27 (12), pp.3679 - 3706. 10.1080/19648189.2022.2146317 . hal-04003908

HAL Id: hal-04003908
https://hal.science/hal-04003908

Submitted on 24 Feb 2023

Simulation of internal and external sulfate attacks of concrete with a generic reactive transport-poromechanical model

Adrien Socié[a,c], Frédéric Dubois[b,c], Yann Monerie[b,c], Mejdi Neji[a], Frédéric Perales[a,c]

[a]Institut de Radioprotection et de Sûreté Nucléaire (IRSN), Cadarache ; [b] Laboratoire de Mécanique et Génie Civil (LMGC), Montpellier; [c] Laboratoire de Micromécanique et Intégrité des STructures (MIST)

ABSTRACT
Chemical reactions can lead to the expansion of the geomaterial because of the strong precipitation of minerals in the pores of the medium. The quantity and the variability of these reactions led to the development of several chemo-mechanical models. A generic chemo-poromechanical model is proposed to predict both the material degradation induced by various concrete pathologies and the environmental multi-factor impact on the macroscopic swelling. The model is based on the coupling between reactive transport (species diffusion and chemical reactions) and poromechanics. The mineralogy and the poromechanical properties are estimated by a hydration-micromechanics model which allows to consider the material effects. The main applications are dedicated to External Sulfate Attack and Delayed Ettringite Formation of cementitious material at mesoscale. The studies highlight the ability of the model to deal with complex and various phenomena such as coupling chemical reactions with calcium leaching, sulfate sorption and ettringite precipitation, and to consider their impact on the macroscopic expansion. Results also bring out the accuracy of the chemo-poromechanical model to simulate different swelling pathologies. The characteristic crack paths induced by differential strain, material impact, and swelling at the macroscopic scale, fit with experimental observations.

KEYWORDS
Sulfate Attacks, Delayed Ettringite Formation, Reactive transport, Expansion, Multiphysics modeling, Poromechanics

1. Introduction

Swelling of geomaterial induced by chemical reactions is a major issue in the prediction of the long term behavior of structures such as bentonite barriers for nuclear waste disposal (Idiart et al., 2020), dam (Lemarchand et al. , 2002; Morenon et al. , 2017), tunnels (Cefis et al. , 2017), or containment building of nuclear power plant (Jabbour , 2018; Marquié et al. , 2019). These reactions are characterized by a strong solid precipitation within pores and cracks. The solid crystallization pressure in the porous medium induces both swelling of the matrix and cracking by differential strain (Gu et al. , 2019; Idiart et al. , 2011; Liaudat et al. , 2020; Martin et al. , 2013). The chemical reactions can be distinguished according to the source of the reactants, internal or external. As explained in the literature, cementitous sample expansions of mature concrete depend on many factors. In the following, we consider three main factors.

(1) **Chemical thermodynamics equilibrium of the main solid**. The swelling reactions are mainly driven by the precipitation of large amount of one solid : alkali

silica gel for alkali silica reaction Lemarchand et al. (2002); Morenon et al. (2017) or ettringite for sulfate attacks Bary et al. (2014); Gu et al. (2022); Sellier & Multon (2018); Tixier & Mobasher (2003). The amount of ions, which can precipitate into the solid, depends on the environment and the initial microstructure. The pH environment changes the electronegativity of the system which impacts the porous medium thermodynamics chemical equilibrium (Neji et al. , 2015; Steefel et al. , 2015). The initial microstructure evolves with the hydration reaction and the clinker composition that impacts the final solid concentration (Bary , 2008; Sellier & Multon , 2018; Tennis & Jenning , 1994; Tixier & Mobasher , 2003). In that way, in sulfate reactions, the amount of tricalcium aluminate plays a major role in the expansion (El Hachem et al. , 2012; Sellier & Multon , 2018; Tixier & Mobasher , 2003). Finally, the moisture (Cefis et al. , 2017; Malbois et al. , 2019) and the temperature (Damidot & Glasser , 1992; Flatt & Scherer , 2008) influence the thermodynamic equilibrium of precipitation.

(2) **Material properties**. Besides the chemical impact on the solid precipitation, the material properties influence the sample expansion (El Hachem et al. , 2012). Indeed, the cement paste properties (mechanical and diffusion) are a function of clinker composition and water cement ratio (Bary , 2008; Bary et al. , 2014). Furthermore, the type, the size and the volume fraction of aggregate impact the final swelling (Al Schamaa et al., 2016).

(3) **Size effect**. The precipitation induced by the species transport leads to a spatial gradient of degradation and stress field. Then, the sample expansion depends on the size of the sample (El Hachem et al. , 2012b; Planel et al. , 2006) and the external loading (Bouzabata et al. , 2012).

To estimate the material aging and the consequences on the reduction of structural performance, models have been developed for the meso- and the macro-scale. Three main types of models are presented in the literature:

(1) **Mechanical modeling**. This kind of modeling focuses on the impact of the swelling area on the material degradation and structural aging (Eddy et al. , 2017; Giorla et al. , 2015; Miura et al. , 2020). These works highlight the effect of the material properties such as the volume fraction of aggregates, but are limited to describe the link with the crack propagation and the swelling kinetic. Furthermore, the swelling is modeled by empirical time functions which are not related to the clinker composition, the pathology or the chemical environment.

(2) **Hydro-mechanical modeling**. In macroscopic modeling, the macroscopic swelling depends on water saturation threshold, kinetic parameters and maximum strain estimated by experimental results (Karthik et al. , 2017; Morenon et al. , 2017). The work of (Martin et al. , 2013) depicts the difficulty to estimate the saturation threshold parameter due to a strong dependence on material properties.

(3) **Chemo-mechanical modeling**. The models are based on thermodynamic chemistry and allow to evaluate the quantity of main solid precipitate and its mechanical impact (Bary , 2008; Bary et al. , 2014; Cefis et al. , 2017; Flatt & Scherer , 2008; Gu et al. , 2019; Idiart et al. , 2011; Qin et al. , 2020; Salgues et al. , 2014; Sellier & Multon , 2018). Models are also able to take into account the variability of the material composition as well as the chemical environment impact. Nevertheless, each model considers only one swelling reaction. In our knowledge, only Gu et al. (2022) applied a similar chemo-mechanical model for two pathologies. Nevertheless, their model does not consider the ions diffusions that mainly impact the estimate crack path and the overall chemo-mechanical degradation at the sample scale.

Our study aims to simulate the degradation of mature cement material by strong solid precipitation. The degradation is thus driven by the local swelling induced by chemical reactions. In that way, the novelty of this study is to propose a generic chemo-poromechanics model where the genericity rests on a specific chemical model for each chemical degradation such as external sulfate attack, delayed ettringite formation, or alkali-silica reaction. The approach is based on reactive hydrogeology (Steefel et al. , 2015) for the chemical part and microporomechanics (Bary et al. , 2014; Sellier & Multon , 2018; Ulm et al. , 2004) for the mechanics modeling.

In that way, the model is based on the coupling between a generic reactive transport model (species diffusion and chemical reaction) and a poromechanical model (poromechanics for swelling and Frictional Cohesive Zone Model for the fracture). Taking into account a reactive transport model allows to simulate the effects of the material composition and the chemical environment on the chemical attack front. The initial concentration and material properties of the mature cement are estimated using a hydration-homogenization model in order to take into account the microstructure. The model is applied at the mesoscale in order to capture the influences of the geometry and the size of the sample on the crack path and the overall chemo-mechanical behavior. The phenomenological model is developed to catch the main factors that affect the sample expansion. The main applications of the paper are External Sulfate Attack (ESA) and Delayed Ettringite Formation (DEF).

This paper begins with a description of the chemo-poromechanical model (section 2). The model rests on the coupling of a reactive transport model, where the species transport and the geochemistry equilibrium model are solved sequentially, and a discontinuous poromechanical model. The chemo-poromechanical applications in section 3 are dedicated to sulfate attacks: External Sulfate Attacks and Delayed Ettringite Formation. Each pathology is distinguished by the source of sulfate and the associated chemical reactions. Note that the mechanical and chemical solvers are the same. These applications bring out the scope and the accuracy of the model. Furthermore, the results fit well with the experimental and literature ones.

2. Chemo-poromechanical model in fractured heterogeneous porous medium

The chemo-poromechanical model is based on the coupling between a poromechanical model and a reactive transport model. One focus on the impact of the swelling, induced by the precipitation of chemical species, on cracking.

The fracture is studied through a micromechanical modeling based on a multibody concept and Frictional Cohesive Zone Model (FCZM) (cf. Figure 1) (Monerie & Acary , 2001; Perales et al. , 2010). Each mesh of finite element modeling is considered as an independent body and the overall behavior is obtained by the coupling of a volume and surface behavior respectively inside and between elements. The volume behavior takes into account the poromechanics and the geochemical behavior of a porous medium without any damage (section 2.2.1). The surface behavior describes the cracks initiation, propagation and post-fracture phenomena (section 2.2.2).

2.1. Reactive transport modeling

The reactive transport model represents the evolution of the mineralogy due to chemical reactions in a fractured concrete. The system is solved by a sequential non-iterative approach (SNIA) with operator splitting method. For each time step, the species transport and the geochemistry equilibrium model are solved sequentially. This article being dedicated to the impact of the chemistry on the concrete swelling, in what follows, the model is briefly described. For more details, see (Socié , 2019; Socié et al. , 2021). Note that here

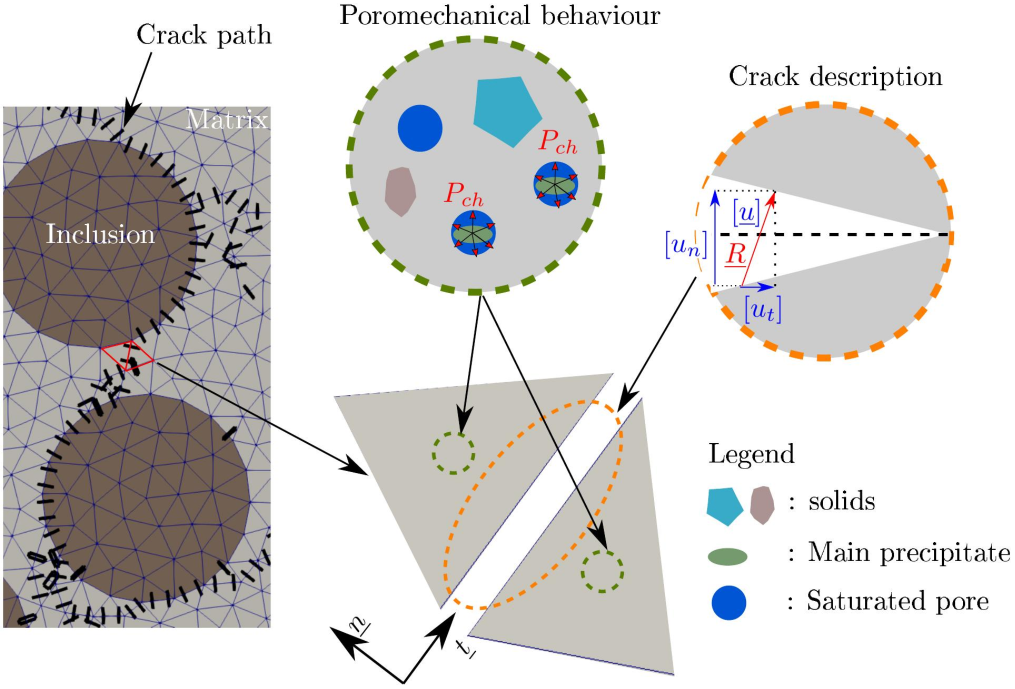

Figure 1. Multibody concept applied to a heterogeneous reactive porous medium. At the gauss points, bulk mechanical processes are integrated. The chemical reaction are described at each nodes. Along the meshes, cracking processes are modeled using a local normal-tangent decomposition.

we assume a constant porosity and no diffusion inside the fracture.

2.1.1. Species transport

The geomaterial is assumed to be fully saturated and the advection phenomenon is not taken into account (Bary et al. , 2014). The transport of the N^{aq} aqueous species is described by the first Fick's law written in terms of concentration:

$$\frac{\partial \phi C_i^{aq}}{\partial t} = \nabla . \left(D_i \nabla C_i^{aq}\right) + \frac{\partial \phi (C_i^{aq})^{\Xi}}{\partial t} \tag{1}$$

where C_i^{aq} $[mol.L^{-1}]$, D_i $[m^2.s^{-1}]$ are respectively the concentration and the effective diffusion coefficient of the species i and ϕ is the porosity $[-]$. The term $\dfrac{\partial \phi (C_i^{aq})^{\Xi}}{\partial t}$ is a source/sink term accounting for the creation/consuming of the ion i in solution as a result of chemical reactions $[mol.L^{-1}.s^{-1}]$.

The species transport modifies the local chemical equilibrium of the system and induces the evolution of the mineralogy.

2.1.2. Geochemistry model

We assume that the chemical processes are at the thermodynamic equilibrium. At mesoscale, the chemical reactions are reversible and are fast enough compared to the species transport. Thus the chemical reactions are supposed to be instantaneous and the kinetic of reactive transport is driven by the species diffusion, as demonstrated by (Samson & Marchand , 2007; Socié et al. , 2021).

In internal swelling reactions, the solid phase depends on the associated precipitation reaction, but also on other chemical reactions such as sorption reaction, initial solids volume fractions or limiting reactant ions concentration (Gu , 2018; Gu et al. , 2022; Liaudat et al. , 2020; Salgues et al. , 2014; Sellier & Multon , 2018). So, we consider three kinds of chemical reactions.

(1) *Aqueous reaction* which is a homogeneous reaction where the products and the reactants are aqueous components. The system is split into $N^{aq,p}$ primary and $N^{aq,s}$ secondary components, which concentrations are respectively denoted $\underline{C}^{aq,p}$ and $\underline{C}^{aq,s}$ (Dieuleveult et al. , 2009; Morel & Morgan , 1972). The secondary aqueous components, products of the reaction, are deduced using the law of mass action of each aqueous reaction:

$$C_i^{aq,s} = \frac{K_i^{aq}}{\gamma_i} \prod_{j=1}^{N^{aq,p}} \left(\gamma_j C_j^{aq,p}\right)^{S_{ij}^{aq}} \tag{2}$$

where K_i^{aq} is the equilibrium formation constant of the aqueous reaction $[-]$ and $\underline{\underline{S}}^{aq}$ is the stoichiometric coefficient matrix of the aqueous reaction $[-]$. The activity coefficient of the ion i, γ_i $[-]$, is expressed by the truncated Davies' law (Neji et al. , 2015; Samson & Marchand , 2007):

$$\begin{cases} I_s = \dfrac{1}{2} \displaystyle\sum_{i=1}^{N^{aq}} z_i^2 C_i^{aq} \\ \ln\left(\gamma_i\right) = -A z_i^2 \left(\dfrac{\sqrt{I_s}}{1+\sqrt{I_s}} - b I_s \right) \end{cases} \tag{3}$$

where z_i is the valence number of the ion i, A and b are parameters.

(2) *Adsorption reaction* which is an heterogeneous reaction involving sorbed and aqueous species. Such as the aqueous components, the sorbed components are split into $N^{ad,p}$ primary, denoted $\underline{C}^{ad,p}$, and $N^{ad,s}$ secondary components, denoted $\underline{C}^{ad,s}$. Based on (Dieuleveult et al. , 2009), we consider the activities of the adsorbed species equal to their concentrations and the secondary components concentrations are deduced using the law of mass action of each absorption reaction:

$$C_i^{ad,s} = K_i^{ad} \prod_{j=1}^{N^{aq,p}} \left(\gamma_j C_j^{aq,p}\right)^{S_{ij}^{ad/aq}} \prod_{u=1}^{N^{ad,p}} \left(C_u^{ad,p}\right)^{S_{i,u}^{ad/ad}} \tag{4}$$

where K_i^{ad} is the sorption equilibrium constant $[-]$, $\underline{\underline{S}}^{ad/ad}$ and $\underline{\underline{S}}^{ad/aq}$ are the stoichiometric coefficients matrices of the sorption reaction $[-]$. The adsorbed concentrations correspond to the quantity of the site sorbed in a mineral.

(3) *Solid reaction* which is a heterogeneous reaction involving solids and aqueous species. Since the solid activity is equal to unity, the solid concentrations cannot be directly deduced by the law of mass action (Erhel & Migot , 2018). The law of mass action condition must be satisfied to ensure the thermodynamic balance of each N^{sol} solid (Erhel & Migot , 2018; Steefel et al. , 2015):

$$\xi_i^{sol}\left(\underline{C}^{aq}\right) \overset{\text{def}}{=} \left(K_i^{sol}\right)^{-1} \prod_{j=1}^{N^{aq,p}} \left(\gamma_j C_j^{aq,p}\right)^{S_{ij}^{sol}} - 1 = 0 \tag{5}$$

where K_i^{sol} is the dissolution equilibrium constant $[-]$, and $\underline{\underline{S}}^{sol}$ is the stoichiometric matrix of the solid reactions $[-]$.

The system is closed by the mass conservation law of the aqueous and the sorbed species:

$$\left\{ \begin{array}{l} \text{find } \underline{C}^{aq,p}, \underline{C}^{ad,p} \text{ and } \underline{C}^{sol}, \text{ such that:} \\ \underline{C}^{aq}_{tot} - \left[\underline{C}^{aq,p} + \left(\underline{\underline{S}}^{aq}\right)^T \cdot \underline{C}^{aq,s} + \left(\underline{\underline{S}}^{ad/aq}\right)^T \cdot \underline{C}^{ad,s} + \left(\underline{\underline{S}}^{sol}\right)^T \cdot \underline{C}^{sol}\right] = \underline{0} \\ \underline{C}^{ad}_{tot} - \left[\underline{C}^{ad,p} + \left(\underline{\underline{S}}^{ad/ad}\right)^T \cdot \underline{C}^{ad,s}\left(\underline{C}^{aq,p}, \underline{C}^{ad,p}\right)\right] = \underline{0} \\ \underline{\xi}^{sol}\left(\underline{C}^{aq,p}\right) = \underline{0} \end{array} \right. \tag{6}$$

where $\underline{C}^{aq}_{tot}$ and $\underline{C}^{ad}_{tot}$ are respectively the total concentration vector of the aqueous species and the sorbed species $[mol.L^{-1}]$, the subscript T define the transpose of the stoichiometric matrix. As considered in the literature (Erhel & Migot , 2018; Lagneau & van der Lee , 2010; Socié et al. , 2021; Steefel et al. , 2015), the measure of the concentration is the molarity which indicates the number of moles of solute per liter of solution. Considering the mass conservation and the mass action of the primary adsorbed species, the multicomponent ion exchange and competitive sorption effects are taken into account. This effect is not considered by the sorption models obtained with the Langmuir or Freundlich formulations (Steefel , 2019). Because the thermodynamic equilibrium is assumed, there is not a linear relationship between the primary components that allows us to obtain the solid concentration like in the kinetic models (Steefel et al. , 2015). The solid concentrations are deduced by solving the overall equations system (6).

Note that some ions do not interact strongly with the porous medium but impact the thermodynamic equilibrium of the solids due to electrostatic effects. (Gu , 2018; Gu et al. , 2022; Neji et al. , 2015; Sellier & Multon , 2018). To take into account this impact, one impose the electroneutrality (Gu , 2018; Gu et al. , 2022; Liaudat et al. , 2020; Neji et al. , 2015; Salgues et al. , 2014):

$$\sum_{j=1}^{N^{aq}} z_j C_j^{aq} = 0 \tag{7}$$

To ensure the positivity of all concentrations, the law of mass action is rewritten in logarithmic form and the system is solved by a Newton algorithm. When the electroneutrality is imposed, the equation 7 replaces a mass conservation law of a primary aqueous species. For more details, see (Socié , 2019; Socié et al. , 2021).

2.2. Poromechanics modeling

2.2.1. Volumetric behavior: poromechanics

In the bulk, the porous medium is described through an isotropic elastic poro-mechanical model (Coussy , 2004):

$$\underline{\underline{\sigma}} = \mathbb{C} : \underline{\underline{\varepsilon}} - bP_{ch}\underline{\underline{I}} \tag{8}$$

where $\underline{\underline{\sigma}}$ is the Cauchy stress tensor $[Pa]$, $\underline{\underline{\varepsilon}}$ is the linearized strain tensor $[-]$, $\mathbb{C}$ is the fourth order stiffness tensor $[Pa]$, b is the Biot coefficient $[-]$, P_{ch} is the pore pressure $[Pa]$, and $\underline{\underline{I}}$ is the identity second order tensor.

In chemo-poromechanics modeling, the pressure use to be proportional to the volume fraction of main solid precipitation such as the silica gel for Alkali Silica Reaction (Lemarchand et al. , 2002; Morenon et al. , 2017) or the ettringite for Delayed Ettringite Formation (Salgues et al. , 2014; Sellier & Multon , 2018). Furthermore, in these models, a volume fraction threshold is introduced and the pressure remains positive. So, based on the second macroscopic state equation, the pore pressure can be written:

$$\left\{ \begin{array}{l} P_{ch} = N \left\langle \varphi_{ms} - \left\langle \varphi^0_{ms} + b tr(\underline{\underline{\varepsilon}}) \right\rangle_+ \right\rangle_+ \\ \varphi_{ms} = \phi V_{ms} C^{sol}_{ms} \end{array} \right. \tag{9}$$

where φ_i and V_i are respectively the volume fraction $[-]$ and the solid molar volume of the solid i $[m^3.mol^{-1}]$, the subscript ms defines the variable associated with the main solid phases, $\langle x \rangle_+ = (x + |x|)/2$, N is the skeleton Biot modulus $[Pa]$ and φ^0_{ms} represents the quantity of initial pores to be filled by the solid to induce swelling $[-]$ which can be related to the microscopic precipitation behavior. According to (Gu et al. , 2022), during a sulfate attacks, the largest pores are partly filled first by ettringite and then the material swelling is induced by the precipitation inside the smallest pore. Note that the Biot's coefficient and modulus are estimated by analytical homogenization and thus the impact of the precipitation source can be considered.

The porosity ϕ depends on the mineralogy evolution such that (Lagneau & van der Lee , 2010; Planel , 2002; Socié et al. , 2021):

$$\phi = 1 - \sum_{i=1}^{N^{sol}} \varphi_i = 1 - \sum_{i=1}^{N^{sol}} \phi V_i C^{sol}_i \quad \Rightarrow \quad \frac{\partial \phi}{\partial t} = - \frac{\displaystyle\sum_{i=1}^{N^{sol}} \phi V_i \frac{\partial C^{sol}_i}{\partial t}}{\left(1 + \displaystyle\sum_{i=1}^{N^{sol}} V_i C^{sol}_i \right)} \tag{10}$$

As a first approximation, the viscoelasticity of the cement paste is not taken into account (Bary , 2008; Bary et al. , 2014; Cefis et al. , 2017; Eddy et al. , 2017; Gu et al. , 2022; Liaudat et al. , 2020; Miura et al. , 2020; Tixier & Mobasher , 2003). Furthermore, the evolution of the porosity only impacts the mechanical model (swelling).

2.2.2. Surface behavior: cracks

Each element is considered as an independent body and an interface law is introduced between each finite element representing the crack (Perales et al. , 2008). A cohesive stress $\underline{R}^{coh}$ $[Pa.m^{-1}]$, is related to the displacement jump of the crack lips $[\underline{u}]$ $[m]$, by a damageable surface second order stiffness tensor $\underline{\underline{K}}(\beta)$ ($\beta = 1$: healthy interface, $\beta = 0$: broken interface). $\underline{R}^{coh}$ and $[\underline{u}]$ are described in the local frame ($\underline{n}$,$\underline{t}$,$\underline{s}$) by their normal and tangential components respectively noted $[\underline{u}] = [u_n]\,\underline{n} + [\underline{u}_{ts}]$ and $\underline{R}^{coh} = R^{coh}_n \underline{n} + \underline{R}^{coh}_{ts}$ (see. Figure 1):

$$\underline{R}^{coh} = \underline{\underline{K}}(\beta) \cdot [\underline{u}] \tag{11}$$

In the Frictional Cohesive Zone Model (FCZM) approach, the cohesive stress is introduced in the Signorini–Coulomb conditions to take into account the cohesive phenomena (Monerie & Acary , 2001):

Signorini conditions:

$$[u_n] \geq 0, \quad R_n + R_n^{adh} \geq 0, \quad [u_n]\left(R_n + R_n^{adh}\right) = 0, \tag{12}$$

Coulomb's laws:

$$||\underline{R}_{ts} + \underline{R}_{ts}^{adh}|| \leq \mu^c |R_n + R_n^{adh}|, \tag{13}$$

where

$$\begin{cases} ||\underline{R}_{ts} + \underline{R}_{ts}^{adh}|| < \mu^c |R_n + R_n^{adh}|, \Longrightarrow \dfrac{\partial [\underline{u}_{ts}]}{\partial t} = 0, \\ ||\underline{R}_{ts} + \underline{R}_{ts}^{adh}|| = \mu^c |R_n + R_n^{adh}|, \Longrightarrow \exists \lambda \geq 0, \; \dfrac{\partial [\underline{u}_{ts}]}{\partial t} = -\lambda \left(\underline{R}_{ts} + \underline{R}_{ts}^{adh}\right), \end{cases} \tag{14}$$

where μ^c is the Coulomb friction coefficient $[-]$ and $\underline{R} = R_n \underline{n} + \underline{R}_{ts}$ is the contact force vector $[Pa.m^{-1}]$ (see Figure 1).

The evolution of the surface stiffness is written as (Perales et al. , 2008):

$$\begin{cases} \underline{\underline{K}}(\beta) = \beta \left(R_n^0 \underline{n} \otimes \underline{n} + R_{ts}^0 \dfrac{[\underline{u}_{ts}] \otimes [\underline{u}_{ts}]}{|| \, [\underline{u}_{ts}] \, ||^2} \right), \\ \beta = \min \left(g(|| \, [\underline{u}] \, ||), g(|| \, [\underline{u}] \, ||_{max}) \right), \\ g(x) = \begin{cases} 1 & \text{if } x \leq [u^c], \\ \dfrac{[u^c]}{x} \left(1 - \left(\dfrac{x - [u^c]}{[u^u] - [u^c]} \right)^2 \right) & \text{if } [u^c] < x < [u^u], \\ 0 & \text{if } x \geq [u^u] \end{cases} \end{cases} \tag{15}$$

where R_n^0 and R_{ts}^0 are respectively the initial normal and tangent surface stiffnesses of the perfect interface $[Pa.m^{-1}]$, $[u^c]$ and $[u^u]$ are respectively the displacement damage at initiation and the ultimate displacement at the onset of the failure (cf. Figure 2). $||[u]||_{max}$ is the maximum value reached by $||[u]||$ during the fracture process.

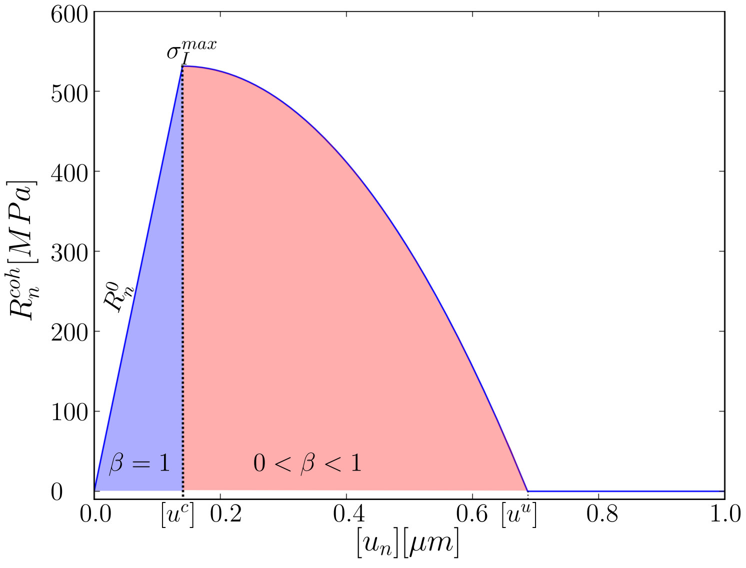

Figure 2. The FCZM normal behavior ($[\underline{u}_{ts}] = 0$)

The initial surface stiffnesses R_n^0 and R_{ts}^0 are deduced from the bulk parameters (isotropic material) and the characteristic mesh length l_c such that (Blal et al. , 2012):

$$R_n^0 \geq \frac{23}{1-\nu}\frac{E}{lc} \qquad R_{ts}^0 = 2\frac{1-2\nu}{1+3\nu}R_n^0 \tag{16}$$

where E is the Young modulus $[Pa]$ and ν is the Poisson coefficient $[-]$.

The values of $[u^c]$ and $[u^u]$ depend on the maximum values of the cohesive stress $(\sigma_I^{max}, \sigma_{II}^{max})$ and the modes I and II fracture energy (w_I, w_{II}) which allow to take into account the mixed mode crack (Bisoffi-Sauve et al. , 2019; Socié , 2019; Venzal et al. , 2020):

$$\begin{cases} [u^c] = \dfrac{\sigma_I^{max}\sigma_{II}^{max}}{R_n^0 R_{ts}^0}\left(\dfrac{1+b_\beta^2}{\left(\dfrac{\sigma_{II}}{R_{ts}^0}\right)^2 + \left(\dfrac{\sigma_I b_\beta}{R_n^0}\right)^2}\right)^{1/2}, \qquad b_\beta = \dfrac{[\underline{u}_{ts}]}{[u_n]} \\ \\ [u^r] = \dfrac{3}{2}\left(\dfrac{w_I w_{II} - \dfrac{[u^c]^2\varpi}{2}}{[u^c]\varpi}\right) + [u^c], \qquad \varpi = \dfrac{w_{II}R_n^0}{1+b_\beta^2} + \dfrac{w_I R_{ts}^0 b_\beta^2}{1+b_\beta^2} \end{cases} \tag{17}$$

where b_β is the displacement ratio.

The crack problem is treated with the Non-Smooth Contact Dynamics (NSCD) approach (Monerie & Acary , 2001; Perales et al. , 2008).

2.3. Chemo-poromechanical modeling

Coupling strategy

The coupling strategy rests on a Sequential Non Iterative Approach (also called Staggered approach). For each time step, one calculates sequentially (Figure 3):

1. **Species transport** (section 2.1.1): the aqueous species concentrations are obtained integrating Fick's law using the chemical state of the previous time;
2. **Geochemistry** (section 2.1.2): the mineralogical modification is estimated by aqueous, solid and sorption reactions from current aqueous species concentrations ;
3. **Poromechanics** (section 2.2.1): the main solid phases evolution leads to the swelling of the bulk and potentially the fracture initiation or propagation.

Characteristic time On one hand, to solve properly the Frictional Cohesive Zone Model problem, the NSCD approach imposes small time step (i.e. around $10^{-6}s$ for our applications) (Monerie & Acary , 2001). On the other hand, the internal swelling reactions are delayed pathologies that can occur up to 300 days (El Hachem et al. , 2012; Gu et al. , 2019; Salgues et al. , 2014; Sellier & Multon , 2018). To keep reasonable computational time, a characteristic time has to be introduced $t_c = at$. The species transport equation 1 becomes:

$$\frac{\partial \phi C_i^{aq}}{\partial t_c} = \nabla.\left(aD_i \nabla C_i^{aq}\right) + \frac{\partial \phi (C_i^{aq})^{\Xi}}{\partial t_c} \tag{18}$$

The physical models are implemented in the XPER (eXtented cohesive zone models and PERiodic homogenization) code (Perales et al. , 2010), which handles general Finite

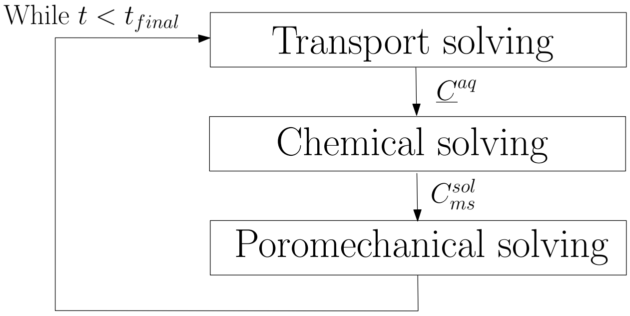

Figure 3. SNIA coupling strategy.

Element tools with parallel computation capability. It is devoted to the study of dynamic fracture of heterogeneous materials with strong multi-physics coupling (Bichet , 2017; Socié , 2019).

Initialization The initial chemo-mechanical parameters are estimated, on the one hand, by a hydration computation to estimate the microstructure and the initial concentrations, and, on the other hand, by analytical homogenization to evaluate the diffusive and poro-elastic parameters (Socié et al. , 2022) (see appendix A). Thus, only the volume fraction φ^0_{ms} is fitted or estimated.

Modular validation The proposed model is based on the coupling of three physical models: a reactive transport model, a poromechanical crack model, and a multiscale-hydration model. The validation is modular, each physical model has been independently validated:

(1) the reactive transport has been benchmarked with the so-called reactive transport code HYTEC (van Der Lee et al. , 2003), see (Socié et al. , 2021);
(2) the cohesive zone model has been the subject of several publications (Bisoffi-Sauve et al. , 2019; Lhonneur , 2021; Perales et al. , 2008; Salah et al. , 2019);
(3) the poromechanical behavior is described in details in (Socié , 2019);
(4) the multiscale validation is depicted in (Socié et al. , 2022).

The proposed study presents a methodology to tackle the simulation of chemical pathology that induces cementitious material swelling and the next section is dedicated to the qualitative validation of the multiphysics coupling.

3. Simulations of sulfate attacks

Swelling of concrete due to Sulfate reactions is characterized by a high concentration of sulfate that induces mainly the precipitation of ettringite. The applications focus on the External Sulfate Attack (ESA) (section 3.1) and Delayed Ettringite Formation (DEF) (section 3.2). These simulations are qualitative applications of the model to a mature homogeneous cement material that focuses on swelling reaction and the associated crack propagation. The chemical modeling focuses on the main parameters, and some approximations have been taken into account in order to reduce the computational time. Furthermore, as previously described in the first part 2.2.1, the model considers only one main solid precipitation and does not consider the impact of secondary solid precipitates, such as gypsum, that could be a source of swelling (Bary et al. , 2014; Bui , 2016) and impact the chemical field (Planel et al. , 2006).

Note that, each application model differs only in the geochemical model and chemical boundary conditions.

3.1. External Sulfate Attack (ESA)

ESA is an external chemical pathology where the sulfate penetrates the concrete from the surrounded medium and leads to ettringite and gypsum precipitation. Sulfate ions are present in groundwater, seawater and geological site (Cefis et al. , 2017; Planel et al. , 2006). Precipitation mainly occurs on surface, leading to differential strain and finally flaking of the concrete structure (Cefis et al. , 2017; Idiart et al. , 2011; Planel , 2002).

3.1.1. Chemical modeling

The chemical model describing ESA takes into account the main ions composing the ettringite solid. To reduce the chemical system, only one solid phase is considered by ions and we do not model second solid phases. For each ions we assume the following phases:

- Portlandite is the main calcium phases,
- The aluminate phase is mainly represented here by the katoite,
- The main sulfate phase is the ettringite.

In first approximation, we do not consider the influence of C-S-H phases on the chemical behavior. The C-S-H are relatively stable in leaching reaction (Socié et al. , 2021), the decalcification occurs when the portlandite is totally dissolved and the C-S-H is degraded on a zone of about 0.1-0.3 mm from the exposed surface (Bary et al. , 2014; Planel , 2002; Soive et al. , 2016). Because of the size of the cement sample simulated (see section 3.1.2), we do not model the C-S-H dissolution. This assumption is also consider by (Gu , 2018; Idiart et al. , 2011; Tixier & Mobasher , 2003). Furthermore, the sorption reaction is not modeled. Indeed, in our knowledge except the work of (Barbarulo , 2002; Soive & Tran , 2017), few reactive transport simulations model the sorption reactions for ESA simulation (Bary , 2008; Bary et al. , 2014; Gu , 2018; Gu et al. , 2022; Planel , 2002; Qin et al. , 2020; Tixier & Mobasher , 2003). Finally, to avoid modeling a large number of aqueous reactions, the electroneutrality condition is imposed and replaces the mass conservation law of the hydroxide species OH^- (Socié et al. , 2021). The chemical reactions, the aqueous components and the equilibrium constant of the porltandite, katoite and ettringite precipitation reaction are described in the Table 1. The thermodynamic database THERMODEM 17 (Blanc et al. , 2012) and CEMDATA (Lothenbach et al. , 2019) are used and the truncated Davie's law parameters (3) are $A = 1.13$ and $b = 0.25$ (Socié et al. , 2021).

Chemical equations			$\log_{10}\left(K^{sol}\right)$
Portlandite	$\Longleftrightarrow$	$Ca^{2+} + 2OH^-$	-5.19
Katoite	$\Longleftrightarrow$	$2Al(OH)_4^- + 3Ca^{2+} + 4OH^-$	-20.5
Ettringite	$\Longleftrightarrow$	$2Al(OH)_4^- + 6Ca^{2+} + 3SO_4^{2-} + 4OH^- + 26H_20$	-44.9

Table 1. Chemical reactions for the External Sulfate Attack simulation (Blanc et al. , 2012; Lothenbach et al. , 2019).

3.1.2. Planel experiments (Planel , 2002)

Planel experiments (Planel , 2002) focus on the free swelling and the degradation of a rectangular parallelepiped cement paste sample ($15 \times 40 \times 160\ mm^3$) submitted to sodium sulfate attack on two thirds of the boundaries.

Following (Planel , 2002), we assume two dimensional plane strain conditions. Due to symmetry, we consider only one quarter of the sample subjected to a chemical loading (Dirichlet boundary conditions) on two-third of the left side (cf. Figure 4). The other boundaries are subjected to free Neumann conditions (no stress and no chemical flux are imposed).

The mechanical loading induced by chemical reactions can be viewed as a thermal loading and thus can lead to a shock (Bary et al. , 2014) and the flaking of the boundary finite elements. As (Bichet , 2017), we consider a non-damageable area with high cohesive properties in a thin band close to the imposed boundary conditions.

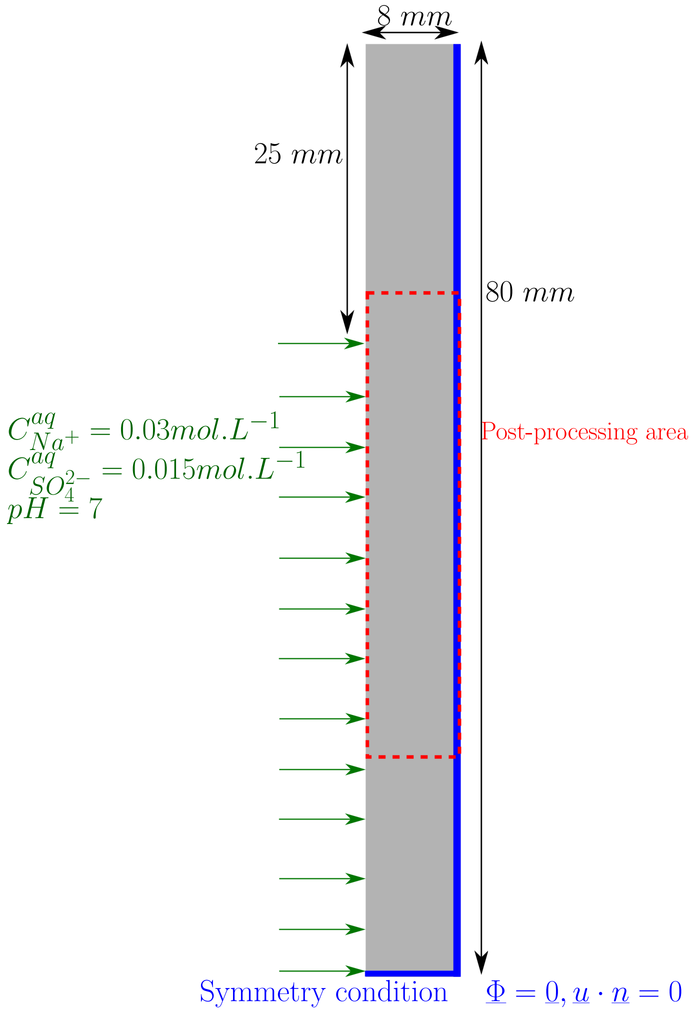

Figure 4. External Sulfate Attack: sketch of the chemical and the mechanical boundary conditions applied to the system (Planel , 2002). $\underline{\Phi}$ is the imposed species flux.

The cement is composed of CEM I 52.5 R Calcia cement, 100% clinker with an additional 6% gypsum, and a water/cement ratio of 0.4 (Planel , 2002). The cement composition is specified in the Table 2.

C_3S	C_2S	C_3A	C_4AF	Additional gypsum
58.4	14.5	9.9	7.1	6

Table 2. Chemical composition (in percent of mass) of cement with a water cement ratio equal to 0.4 (Planel , 2002) .

The Table 3 and 4 describe respectively the initial chemical properties and the material parameters estimated by a hydration model (see Appendix A) from the cement composition (Planel , 2002; Planel et al. , 2006). The mechanical parameters fit well with the experimental measurements, but the porosity and the Young's Modulus are respectively underestimated and overestimated. The difference could be explained by the fact that the hydration computation considers a total hydrated cement. Furthermore, we assume the cement paste is composed of katoite and ettringite which admits a higher volume fraction than a system composed of monosulfoaluminate and ettringite. The cohesive parameters are described in the Table 5. The maximum value of the normal cohesive stress corresponds to a tensile strength of $3MPa$ (Bichet , 2017; Socié , 2019), commonly chosen for mortar or cement paste (Eddy et al. , 2017; Giorla et al. , 2015; Idiart et al. , 2011; Socié , 2019). In mode II, the cohesive stress and fracture energy is considered to be 10 times higher than the first mode as reported by (Idiart et al. , 2012, 2011; Socié , 2019) The chemical time step is 1 minute and the mechanical time step is 10^{-7} minutes (with $a = 10^7$ in (18)). The characteristic mesh size is about $0.3mm$.

Solid phase		Aqueous species	
Species	Volume fraction	Species	Concentration $[mmol.L^{-1}]$
C-S-H	0.369	SiO_2	8.7×10^{-4}
Portlandite	0.189	Ca^{2+}	17.
Ettringite	0.144	SO_4^{2-}	1.1×10^{-3}
Katoite	0.072	$AlOH_4^-$	8.5×10^{-2}
Calcite	0.026	OH^-	34
ϕ	0.2		

Table 3. External Sulphate Attack: initial chemical parameters for the cement paste composition described in (Planel , 2002). Note that the C-S-H and the silica aqueous species are not taken into account in the sulfate attack simulation.

	$E\ [GPa]$	$\nu\ [-]$	$b\ [-]$	$N\ [GPa]$	$\varphi_{ms}^0\ [-]$	$D\ [m^2.s^{-1}]$
Estimated values	24.06	0.253	0.123	101.513	0.16	2.73×10^{-12}
Experimental values	20	0.2	-	-	-	$[4.3 \times 10^{-13}, 2.3 \times 10^{-12}]$

Table 4. External Sulphate Attack: initial mechanical parameters estimated for the cement paste composition described in (Planel , 2002).

Interface	$\sigma_I\ [Pa]$	$\sigma_{II}\ [Pa]$	$w_I\ [J.m^{-2}]$	$w_{II}\ [J.m^{-2}]$
matrix-matrix	46×10^6	46×10^7	20	200

Table 5. External Sulphate Attack: cohesive parameters (Bichet , 2017; Socié , 2019).

The Figure 5 shows the solid concentrations fraction in the first millimeters. As described by various authors (Bary et al. , 2014; Planel et al. , 2006; Qin et al. , 2020; Soive et al. , 2016; Soive & Tran , 2017), on the one hand, the ettringite precipitation induces the dissolution of the aluminate phase and on the other hand, the low pH environment leads to the portlandite dissolution. The maximum ettringite value depends on the initial concentration of katoite which is the limiting reactant of the reaction.

The evolution of the porosity according to the different solid phases (see (10)) impacts the volume fraction of the main precipitate and so the pressurization of the medium (see (9)). In the literature (Bary , 2008; Bary et al. , 2014), the porosity dependency is generally introduced through the Young's modulus with similar swelling effects. To illustrate the strain effect, one can write the strain from the elastic poro-mechanical model (8) in one dimension:

$$\sigma = E\varepsilon - bP = 0 \Longleftrightarrow \varepsilon = \frac{bP}{E} \tag{19}$$

Considering a Representative Volume Element without any external loading, a constant pressure and a Young Modulus decreasing with respect to the porosity, the strain increases. Note that the porosity is constant in the reactive transport solver and the porosity evolution only impacts the solid volume fraction and therefore the mechanical swelling.

The model takes into account the impact of the chemical reactions coupling, here the calcium leaching and the ettringite precipitation, on the mechanical loading (Bary , 2008; Bary et al. , 2014; Qin et al. , 2020). Because the initial solid volume fractions are estimated by the hydration computation and the aluminate phase constitutes the limiting reactant of the ettringite precipitation, the model accurately takes into account the influence of the clinker mineralogy on the macroscopic expansion (Socié , 2019).

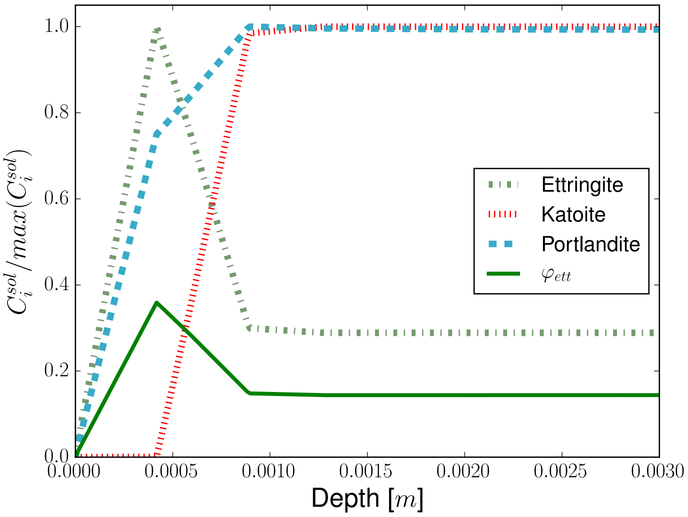

Figure 5. External Sulphate Attack: solid concentrations fraction, ettringite volume fraction and porosity at 70 days. Abscissa 0 corresponds to the boundary.

The gradient of the precipitation field induces a swelling gradient in the sample and degradation by differential strain. The Figure 6 shows the evolution of the crack width and the ettringite concentration field at different times. As described experimentally by (Planel , 2002) and numerically by (Bary , 2008; Bary et al. , 2014), four degradation steps are highlighted:

- step 1: a crack initiates between the chemical attack zone/loading zone and the internal safe zone due to differential strain,
- step 2: the crack propagates from the boundary towards the central part of the sample,
- steps 3 and 4: several cracks initiate on the interface between the attack and the safe zones, and propagate to the center with an angle around 45° with the top boundary. Cracks coalescence occurs and create a crack parallel to the boundary conditions. The two kinds of cracks shapes are observed experimentally by (Planel , 2002).

The model is able both to capture the local swelling effects such as the shearing between the safe and the degraded zones and to reproduce the specimen behavior.

3.1.3. Conclusion

The developed approach can model the combined effects of both external sulfate reaction and calcium leaching on the chemistry and on the swelling of the cement paste. The crack initiation is due to the local differential strain between the chemical attack zone and the safe material. Then, the crack propagation is influenced by the local swelling and macroscopic sample expansion. The simulation highlights the importance of mesoscale simulations to distinguish the local material effect from the one induced by the macroscopic sample deformation.

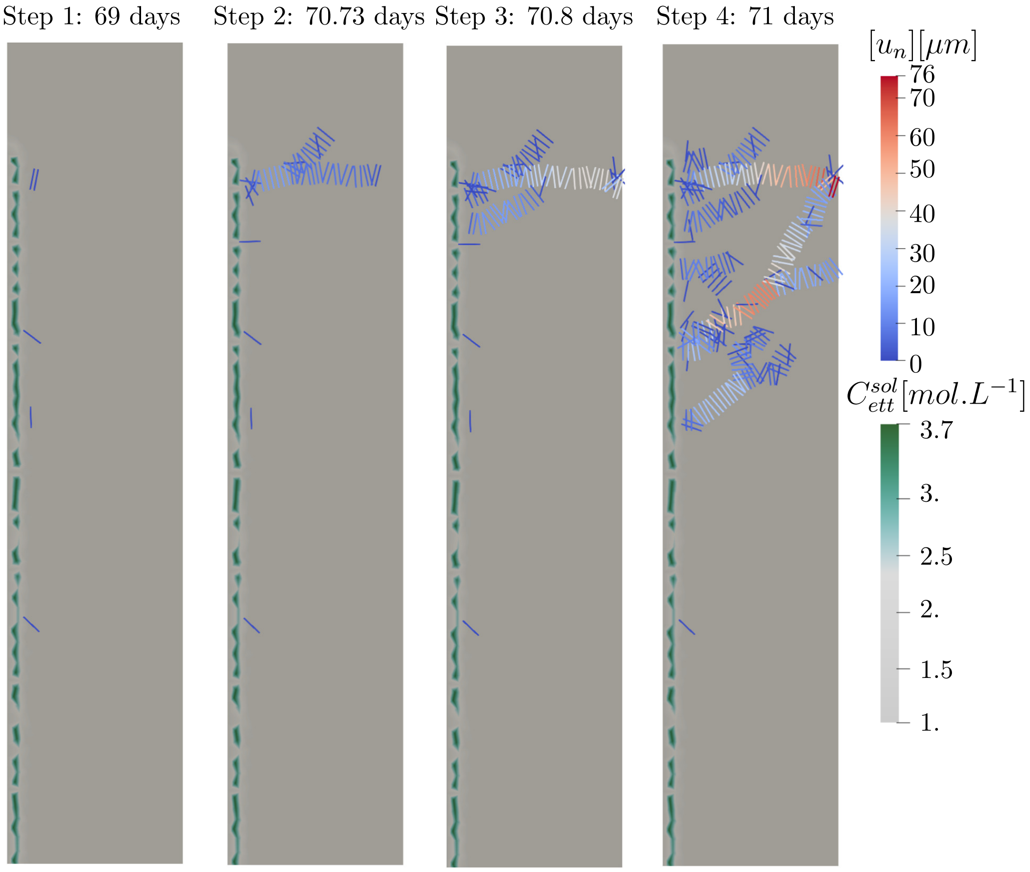

Figure 6. External Sulfate Attack: displacement jump or crack width (blue to red) and ettringite concentration (green) for the four main times.

3.2. Delayed Ettringite Formation (DEF)

DEF is an endogenous pathology due to a significant warm-up of a particular cement composition. The curring condition induces the dissolution of primary sulfoaluminate hydrates. Some hydrate's components, as sulfate, are sorbed by C-S-H. In contact with a moisture environment, sulfate ions are desorbed and ettringite can precipitate in voids and cracks (Divet & Randriambololona , 1998; Malbois et al. , 2019; Salgues et al. , 2014; Sellier & Multon , 2018).

This application focuses on the modeling of the degradation of a mature mortar induced by the delayed ettringite formation. The model does not consider the physical-chemistry reaction during the excessive heating, but consider an initial concrete where a part of sulfate ions are sorbed. The great uncertainty associated with the initial mortar composition leads to a qualitative simulation.

Note that only the chemical modeling of DEF application is different of ESA application. The mechanical and chemical solvers are the same. This application underlines the modeling genericity and the capacity of the model to simulate a large number of swellings reactions.

3.2.1. Chemical modeling

As described by (Gu et al. , 2022; Sellier & Multon , 2018) (Gu , 2018; Martin et al. , 2013; Salgues et al. , 2014), the DEF chemo-mechanical model has to take into account the link between the sulfate sorption and the sodium leaching. In that way, we add to the ESA chemical model (cf. section 3.1.1) the sorption of sulfate with main anions in solution, i.e. calcium sulfate $CaSO_4^-$ and sodium sulfate $NaSO_4^{2-}$ (Irbe et al. , 2019). The reactions and the associated equilibrium parameters are described in the Table 6. Based on (Haas & Nonat , 2015; Irbe et al. , 2019; Soive & Tran , 2017), the silanol (denoted $\equiv Si - OH$) is considered to be the only surface site of C-S-H phase and main sorbed component of the model. Note that the equilibrium coefficient considered for the sorption of the calcium sulfate by C-S-H in our applications is the mean value used in (Irbe et al. , 2019; Soive & Tran , 2017). Finally, in first approximation, we do not consider the surface potential of C-S-H such as (Bradbury et al. , 2005; Dieuleveult et al. , 2009).

Chemical equation	$\log_{10}\left(K^{ad}\right)$
$\equiv Si - OH + Ca^{2+} + OH^- + SO_4^{2-} \Longleftrightarrow \equiv Si - OCaSO_4^- + H_2O$	7.3
$\equiv Si - OH + Na^+ + OH^- + SO_4^{2-} \Longleftrightarrow \equiv Si - ONaSO_4^{2-} + H_2O$	5.8

Table 6. Equilibrium sorption constant used for the DEF simulation (Haas & Nonat , 2015; Irbe et al. , 2019; Soive & Tran , 2017).

3.2.2. Free swelling of a cylindrical mortar samples

The application deals with the free swelling of a $11 \times 22\ cm^2$ cylindrical mortar samples. As experiments (Al Schamaa et al., 2016; Gu , 2018; Jabbour , 2018), the samples are immersed in low pH environment to speed up the reaction. Due to symmetry, we simulate only one quarter of the sample (cf. Figure 7). A concentration of $10^{-7}\ mol.L^{-1}$ is imposed for hydroxide OH^- and sodium Na^+ and null for others.

The mortar is based on the one called "$d510p30$" in (Al Schamaa et al., 2016) which corresponds to a volume fraction of limestone filler of 0.3 and a water-cement ratio of 0.37. The hydration computation is solved in two steps:

(1) one hydration computation such as presented in the section A.1,
(2) a thermodynamic simulation considering the microstructure previously estimated but where the ettringite is totally dissolved. The sorption reactions described in 3.2.1 are considered.

Due to the uncertainties in the estimation of the ITZ volume fraction from the size of the sand and the ITZ thickness (Garboczi & Bentz , 1997; Honorio et al. , 2016), we assume a constant value of 0.25. The sand is considered as a no reactive and no diffusive phase.

The initial mechanical and chemical parameters are described in the Table 7, 8 and 9. The cohesive parameters are described in the Table 5. We observe in Table 8 that a low quantity of sulfate is sorbed and a low quantity of ettringite is dissolved. Some uncertainties on the thermodynamic sorption coefficients can explain this result. Furthermore, the microstructure estimation does not take into account the influence of the curring time on the chemical reactions (for example: effect of the curring time on the hydrogarnet siliceous) and the thermo-chemo-mechanical damage behavior of concrete at early age that influence

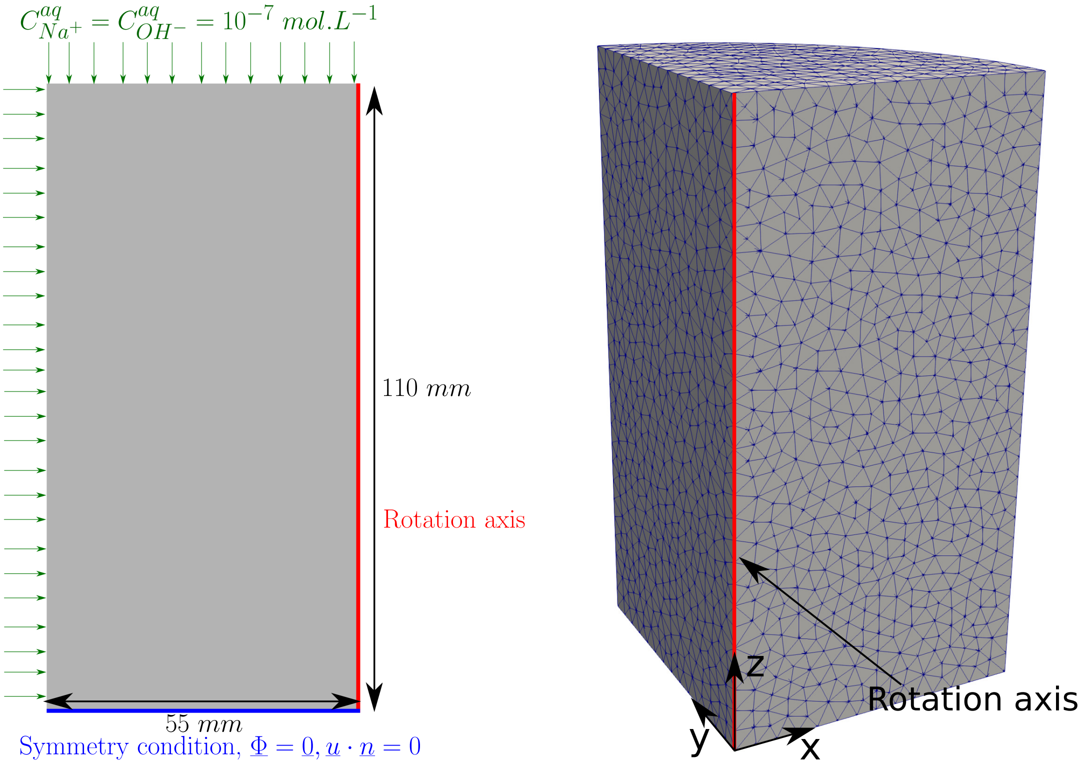

(a) (b)

Figure 7. Delayed Ettringite Formation application: a) sketch of the chemical and mechanical boundary conditions and b) mesh.

the final expansion (Salgues et al. , 2014; Sellier & Multon , 2018). In that way, the estimation of the total porosity is 18.8% that is well below than the one reported by Al Schamaa et al. (2016).

In this study, we focus on the influence of the initial quantity of pore to be filled φ^0_{ms} on the mechanical response (9). Based on the initial porosity $\phi(t_{ini})$, the initial volume fraction of ettringite $\varphi_{ett}(t_{ini})$, sulfate sorbed concentration $C^{ad}_{NaSO_4^{2-}}(t_{ini})$ and using the equation (9), we approximate the maximum value of φ^0_{ms} to assure a macroscopic swelling in our simulations:

$$\varphi^0_{ms} < \varphi_{ett}(t_{ini}) + \frac{C^{ad}_{NaSO_4^{2-}}(t_{ini})\phi(t_{ini})V_{ett}}{3} \tag{20}$$

This value is around 0.098. To study the sample expansion and degradation we consider three values: 0.094, 0.095 and 0.096.

The chemical time step is 60 minutes and the mechanical time step is 6x10^{-8} minutes (with $a = 10^7$ in (18)). The characteristic mesh size is $4mm$.

$E\ [GPa]$	$\nu\ [-]$	$b\ [-]$	$N\ [GPa]$	$\varphi^0_{ms}\ [-]$	$D\ [m^2.s^{-1}]$
26.2442	0.244	0.229	104.851	$[0.095, 0.096, 0.097]$	3.18×10^{-12}

Table 7. Delayed Ettringite Formation application: mortar mechanical parameters

Chemical evolution The Figure 8 shows the evolution of concentration, scaled by the initial value $(C_i)_{ini}$, of the main phases along the abscissa on the rotation axis at day 538. For the sake of readability, the calcium sulfate complex is scaled by $4(C_i)_{ini}$.

First hydration computation

Solid species	Volume fraction
C-S-H	0.364
Portlandite	0.242
Ettringite	0.143
Katoite	0.0236
Calcite	0.03
ϕ_{cp}	0.197

Second hydration computation: solid properties

Solid species	Volume fraction	Aqueous species	Concentration $[mmol.L^{-1}H_2O]$
C-S-H	0.364	Ca^{2+}	0.562
Portlandite	0.248	SO_4^{2-}	1.6×10^{-3}
Ettringite	0.1327	$AlOH_4^-$	1.
Katoite	0.0269	OH^-	294.
Calcite	0.03	Na^+	294.
ϕ_{cp}	0.197		

Table 8. Delayed Ettringite Formation application: cement paste composition, initial chemical parameters estimated by hydration computation estimated from the cement composition of (Al Schamaa et al., 2016).

Solid species	Volume fraction	Sorbed species	concentration $[mol.L^{-1}H_2O]$
C-S-H	0.2415	$\equiv Si - OH$	19.99
Portlandite	0.1645	$\equiv Si - OCaSO_4^-$	3.5×10^{-3}
Ettringite	0.088	$\equiv Si - ONaSO_4^{2-}$	0.233
Katoite	0.0178		
ϕ	0.188		

Table 9. Delayed Ettringite Formation application: initial mortar composition.

As observed in the ESA simulations, the precipitation of the ettringite induces the dissolution of the katoite. Nevertheless, the limiting reactant is not the katoite but the sorbed sulfate ($\equiv Si - ONaSO_4^{2-}$). The ettringite precipitation is due to the desorbed sulfate induced by the sodium leaching (Irbe et al. , 2019; Salgues et al. , 2014; Sellier & Multon , 2018). This leaching destabilizes the chemical equilibrium of the sodium sulfate and induces the desorption of the phases. The released sulfate can be fixed to C-S-H by the sorbed calcium sulfate complex ($\equiv Si - OCaSO_4^-$) or by the precipitated ettringite. The localization of the sulfate depends on both the ions concentration and the electronegativity. Thus, the ettringite precipitation does not only depend on the sodium leaching and, unlike the ESA simulations, the maximum value of the ettringite is not reached on the surface. This effect is a consequence of the low pH environment that induces the dissolution of the portlandite and advantages the sulfate capture by the calcium sulfate complex.

At the time t, the mass of mortar $m(t)$ $[kg.m^{-3}]$ is estimated from the discrete arithmetic mean of solid concentration in a saturated porous medium:

$$m(t) = \frac{1}{NbN} \sum_{j}^{NbN} \left(\sum_{i}^{N^{sol}} C_i^{sol}(t,j) V_i \rho_i^{sol} \phi(t_{ini}) + \rho_s \varphi_s + \rho_w \phi(t_{ini}) \right) \tag{21}$$

where $\underline{\rho}^{sol}$ is the solid density $[kg.m^{-3}]$, NbN is the number of nodes, ρ_s is the sand mass density, ρ_w is the water mass density and φ_s are the volume fraction of sand. The mass is estimated trough the initial porosity, $\phi(t_{ini})$, to isolate the variation of the mass

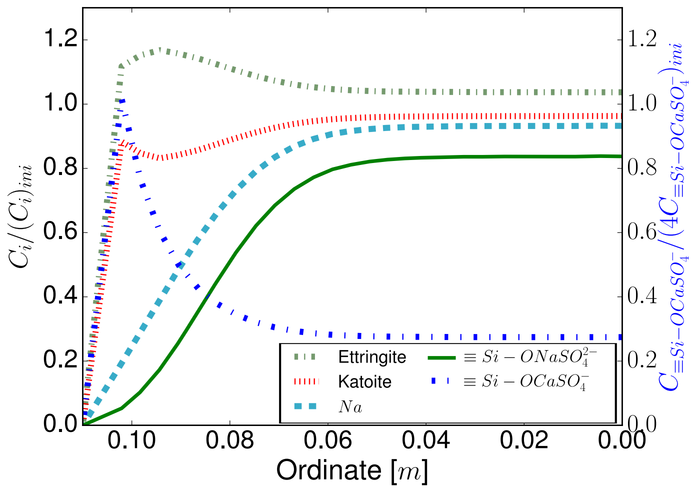

Figure 8. Delayed Ettringite Formation application: concentrations of the main phases scaled by their initial values along the abscissa of the rotation axis at day 538.

by the concentration change. The densities used for the post-processing are sum up in the Table 10.

Portlandite	Ettringite	Katoite	C-S-H	sand
2241.13	1766.93	2530.93	2318.	1600.

Table 10. Densities of the main cement hydrates $[kg.m^{-3}]$ Thermoddem 2017 (Blanc et al. , 2012).

Figure 9 shows the relative mass variation of the samples simulated and experimentally measured. The nomenclature for the experimental results is (Al Schamaa et al., 2016): $dxpy$ where x and y correspond respectively to the mean diameter in μm and the percentage of sand filler. The estimated relative mass variation fit quite well with the experimental result. Two parts of the curve can be distinguished. Firstly, the mass variation increases linearly with respect to time due to the sodium leaching and induces a constant kinetic rate of average ettringite precipitation. Indeed, in the Figure 8, the ettringite concentration is greater than its initial concentration in all the samples. Secondly, the ettringite is more localized near the surface of the samples which reduces the kinetic of the mass evolution. The underestimation of the relative mass at the end of the simulation can be explained by the impacts on the estimated mass change of the porosity evolution, the water consumption or production due to chemical reactions (Seigneur et al. , 2018) and the presence of cracks.

Mechanical response Figure 10 shows the ettringite and the first strain invariant fields at 519 days for $\varphi^0_{ms} = 0.095$. We observe a compression state in the attacked zone and a traction state in other areas. As observed in the ESA simulations, the ettringite induces swelling into the sample and shearing in the corner.

The Figure 11 shows the macroscopic expansion for three threshold volume fractions φ^0_{ms}. The macroscopic expansion is calculated using the strain on the top of the samples. The numerical results are compared to the experimental expansion of three mortar characterized by the diameter of the sand (Al Schamaa et al., 2016). We underline that the expansion fits quite well with the experimental results, despite the great incertitude of the hydration computation. The inflection of the curve corresponds to the crack initiation (at 210 days for $\varphi^0_{ms} = 0.094$ and 515 days for $\varphi^0_{ms} = 0.095$). At this point, an acceleration of the macroscopic expansion is observed. The crack initiation being induced by the swelling gradient, the smaller the threshold volume fraction φ^0_{ms}, the sooner the crack initiates. As

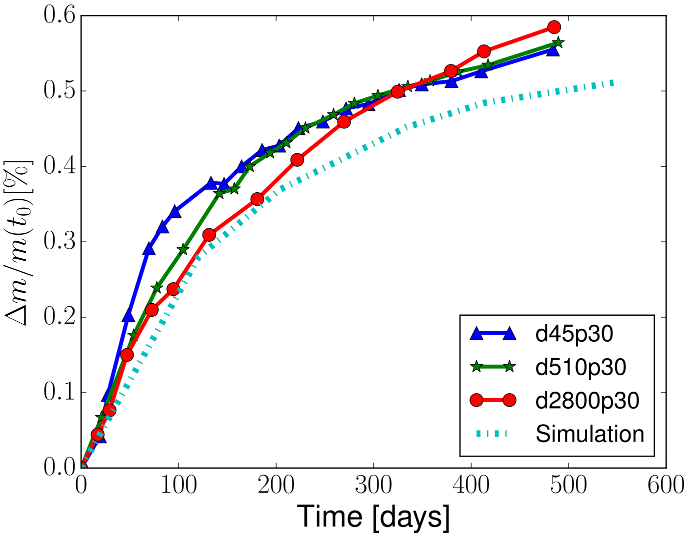

Figure 9. Delayed Ettringite Formation reaction: evolution of the relative mass of experimental (Al Schamaa et al., 2016) and numerical mortar samples.

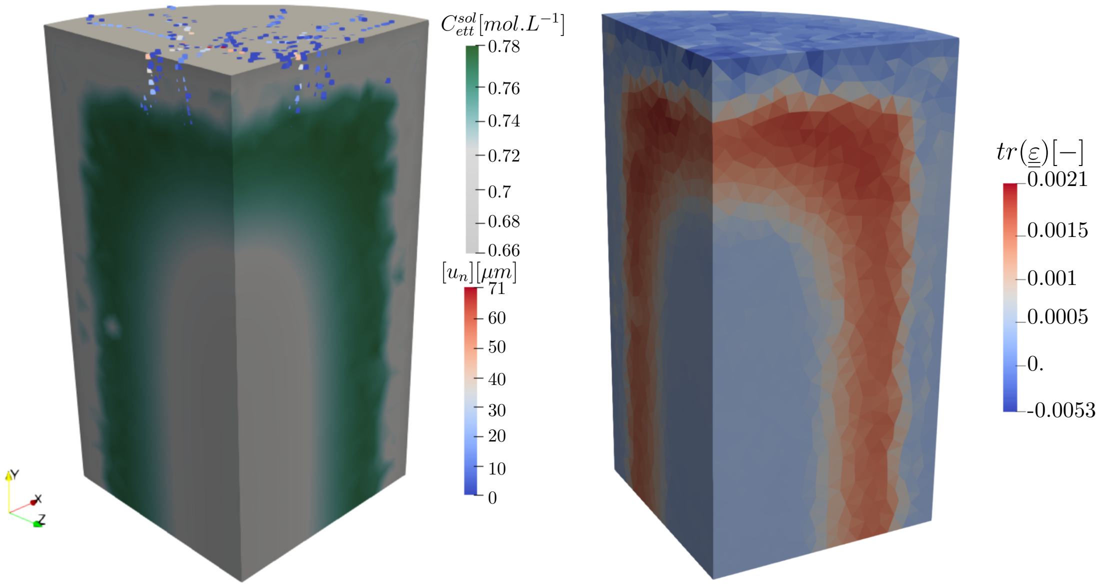

(a) (b)

Figure 10. Delayed Ettringite Formation reaction for $\varphi_{ms}^0 = 0.095$ at 519 days: a) ettringite concentration (green), the minimum value is scaled by the initial ettringite concentration and gap (blue to red), b) first strain invariant.

described in different works (Bary et al. , 2014; Martin et al. , 2013), an expansion threshold parameter impacts not only the initial macroscopic expansion but also the crack propagation. For $\varphi_{ms}^0 = 0.094$ and $\varphi_{ms}^0 = 0.095$, the crack initiates and propagates through the sample. For $\varphi_{ms}^0 = 0.096$, the expansion begins later than the other values, evolves linearly with time and at day 600, the sample remains undamaged.

The threshold volume fraction influences the global response of the system, and takes into account some coupling behavior between mechanics, reactive transport and material characteristic.

Figure 12 shows the evolution of the crack path for $\varphi_{ms}^0 = 0.095$. Due to strain gradient, the cracks initiate on the top face of the sample, propagate on the face then inside the

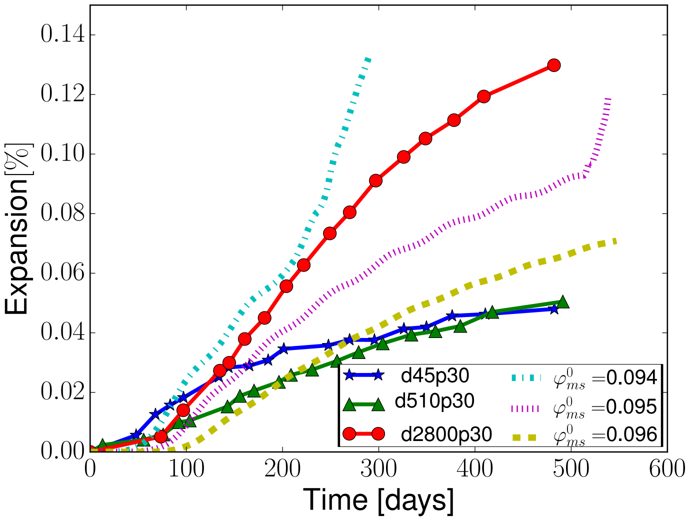

Figure 11. Delayed Ettringite Formation reaction: impact of the threshold volume fraction φ^0_{ms} on numerical expansion and comparison with experimental expansion (Al Schamaa et al., 2016).

sample. Finally, some cracks initiate in the center of the sample and propagate circumferentially due to structural effects. The crack path on the surface agrees with experiments (Kchakech , 2016). The crack path inside the sample is also in accordance with the 2D simulation of (Sellier & Multon , 2018), but our simulation estimates less circumferential cracks.

3.2.3. Conclusion

The Delayed Ettringite Formation application highlights that the generic multiphysics approach can model several a different sulfate reactions by changing only the chemical model and keeping the poromechanical model. The DEF model has been tackled by an original thermodynamics chemical model based on sulfate desorption and ettringite precipitation depending on the local sodium-calcium concentration. The precipitated ettringite, on the one hand, increases the sample's mass, which is in agreement with the experimental values, and, on the other hand, leads to both mortar expansion and mechanical degradation. As the ESA, the results of macroscopic behavior depends on the chemical boundaries conditions that induces local cracks on the surface of the sample and leads to circumferential and center cracks. In accordance with experimental observations, the cracking is more diffuse than for ESA.

4. Discussion of the local swelling induced by chemical reactions

Both applications highlight that the macroscopic expansion depends on the reactive transport evolution as well as on the mechanical response of the sample. The last application depicts that the local material behavior influences the overall chemo-mechanical response of the sample. In this section, we outline the challenges and the limitations associated with the expansion model.

First of all, in our model, it is assumed that the swelling can be quantified from the volume fraction of the main product. This hypothesis is mainly used in the model literature as depicted in the Table 11. Nevertheless, this assumption has been challenged by several papers as (Kunther et al. , 2013) and by models based on the crystallization pressure theory (Flatt & Scherer , 2008; Gu et al. , 2022). The crystallization pressure theory considers

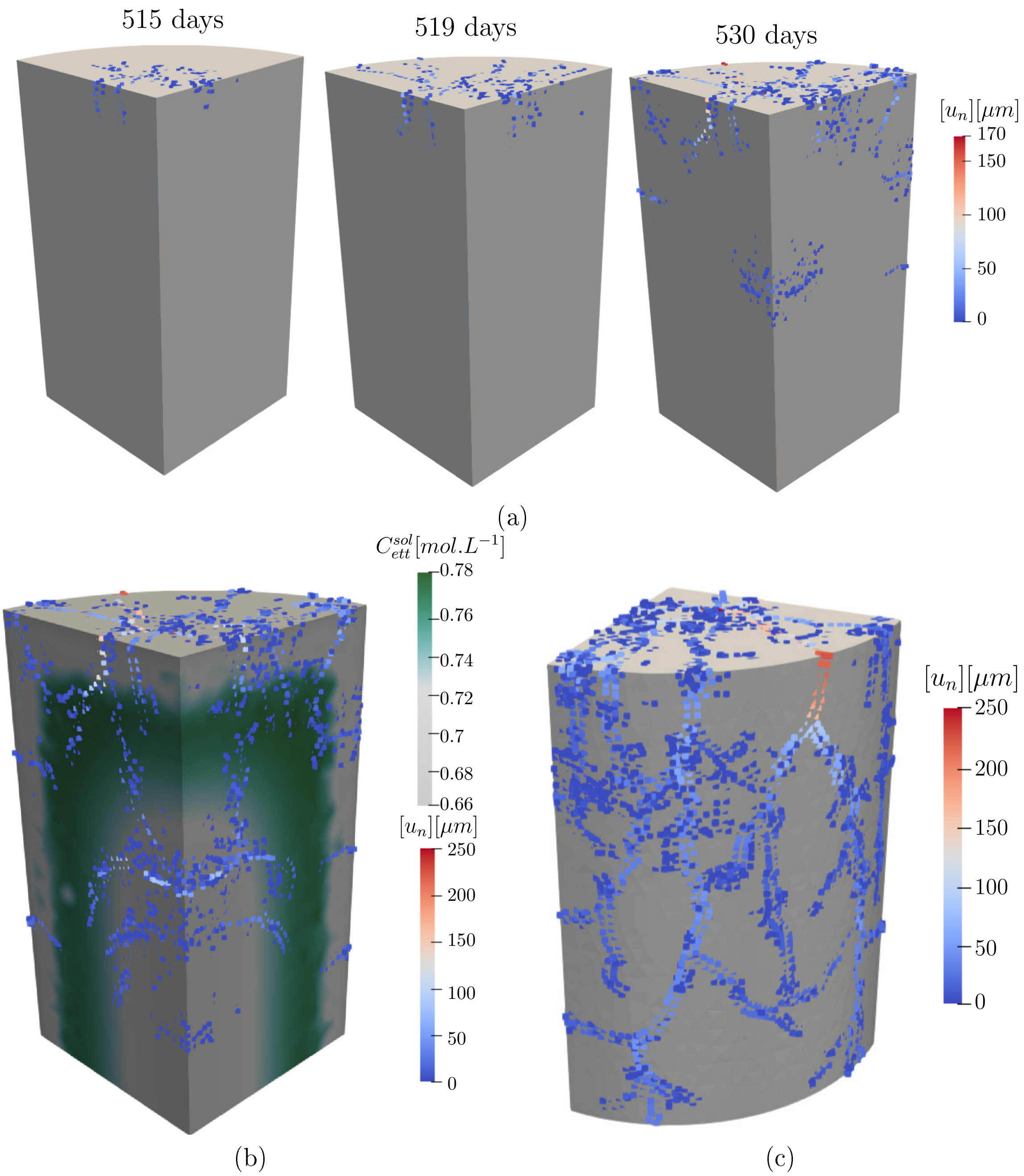

(a)

(b)

(c)

Figure 12. Delayed Ettringite Formation reaction for $\varphi_{ms}^0 = 0.095$: a) evolution of the crack path, b) ettringite field and crack path in the volume at 538 days and c) crack path on external face at 538 days.

that the solid pressure is proportional to the chemical supersaturation:

$$P^c = \frac{RT}{V_{ms}} \log \left((K_i^{sol})^{-1} \prod_{j=1}^{N^{aq,p}} \left(\gamma_j C_j^{aq,p} \right)^{S_{ij}^{sol}} \right) \tag{22}$$

As depicted in the equation (5), the assumption of thermodynamical equilibrium based on the overall reactive transport kinetic (Samson & Marchand , 2007; Socié et al. , 2021) and used by several authors (Dieuleveult et al. , 2009; Erhel & Migot , 2018; Steefel et al. , 2015), is not consistent with the crystallization theory because the associated pressure must be negligible. In that way, the homogeneous concentration related to the reactive transport theory is not emphasized with some multiscale theories depicted in the literature.

Expansion/Pressure related to the volume fraction	Crystallization pressure
(Idiart et al. , 2011; Tixier & Mobasher , 2003) (Bary et al. , 2014; Cefis et al. , 2017) (Miura et al. , 2017; Planel , 2002) (Miura et al. , 2020) (Sellier & Multon , 2018) (Malbois et al. , 2019) (Martin et al. , 2013; Salgues et al. , 2014)	(Bary , 2008) (Flatt & Scherer , 2008) (Gu et al. , 2022)

Table 11. Summary of the main swelling behavior models of the literature.

Secondly, considering that the expansion is related to the volume fraction, the volume fraction threshold, φ^0_{ms}, evolves here with the porosity and so, for example, the pressure increases with the porosity. Nevertheless, the void evolution could have a reservoir role reducing the overall swelling. This porosity also affects the leaching and precipitation front (Lagneau & van der Lee , 2010) which impacts the overall swelling kinetic and heterogeneity. Note that the porosity must be impacted by the solid deformation (Kadeethum et al. , 2021) but the effect remains in second-order (variation around $\simeq 10^{-3}$) compared to the precipitation/dissolution (variation around $\simeq 10^{-1}$). Furthermore, the dissolution and precipitation of hydrated mineral must release and consume water that impact both the reactive transport kinetic (Seigneur et al. , 2018) and the poromechanical behavior (Cefis et al. , 2017).

Finally, cracks accelerate the species transport and lead to the localization of the chemical degradation (Idiart et al. , 2011; Socié et al. , 2021). Solid precipitation inside the fracture induces the pressurization of the crack but also limits the matrix swelling due to the reservoir role of the discontinuity (El Hachem et al. , 2012; Liaudat et al. , 2020). These combined phenomena induce the macroscopic swelling kinetic increase with the initial damage (Leklou et al. , 2012) and the crack propagation (Idiart et al. , 2011; Martin et al. , 2013). Thus, as further chemo-mechanical models specified (Martin et al. , 2013; Salgues et al. , 2014), our model is limited to reproduce the kinetic of degradation due to a low description of the crack behavior.

The numerical method proposed in our work leads to improve and validate each physics independently. For example, the chemical degradation front can be compared to experimental measures before any damage. Subsequent works will be dedicated to couple the crack propagation to our reactive transport model in a porous medium (Socié et al. , 2021).

5. Conclusions

A strong mineral precipitation in a geomaterial can induce the swelling of the structure and its degradation. The swelling sample expansion depends on multi factor: the thermodynamical chemical equilibrium, the material properties and the size of the sample. To predict the main impact of the microstructure and the chemical environment in the sample expansion, a generic chemo-poromechanical model, applied to mesoscale, has been implemented in the XPER software (Perales et al. , 2010). The model relied on the coupling between a poromechanical model and a reactive transport model (species transport and chemical reactions). Fracture was studied through a micromechanical modeling based on a multibody concept and Frictional Cohesive Zone Model (FCZM) (Monerie & Acary , 2001; Perales et al. , 2008, 2010). The genericity of the reactive transport model allowed to simulate a large number of chemo-mechanical expansion, the environmental effect, the cement mineralogy and to model coupling chemical reactions and their impact in the expansion.

The poromechanical model takes into account the heterogeneity of the main solid field and allows to simulate both the concrete swelling and the fracture behavior. The effect of the clinker composition on the swelling kinetics rests on the estimation of the initial chemical and mechanical properties thanks to a hydration-homogenization computation.

The chemo-poromechanical applications dealt with two kinds of sulfate reactions: External Sulfate Attack (ESA) and Delayed Ettringite Formation (DEF). The studies highlighted the ability of the model to deal with complex and various phenomena such as the impact of sodium concentration on the mineralogy and the effect of various limiting reactant (aluminate solid phases for ESA and initial sulfate sodium sorbed for DEF). For the External Sulfate Attack, the estimated crack path agreed well with the experimental observations (Planel , 2002). A first proposition of chemo-mechanical of DEF model at mesoscale was proposed. The chemical model showed the impact of the sodium leaching in the sulfate desorption and the ettringite precipitation. The chemical behavior represented well the evolution of the mass. The poromechanical behavior was studied through the impact of the volume fraction threshold in the macroscopic response. The main mechanical tendency (cracks path and macroscopic expansions) fitted with the literature (Al Schamaa et al., 2016; Sellier & Multon , 2018). The chemical modeling considers one solid phase by ions to represent the main tendency of each swelling reactions. Further applications will be dedicated to increasing the complexity of the chemical model, such as simulating the gypsum, monosulfoaluminate and C-S-H behavior.

Finally, as depicted in the discussion part, several studies have been planed in order to improve the quantitative estimation of the macroscopic swelling based on a fully phenomenological model. Among other, the chemo-poromechanical will be improved to couple the crack propagation to our reactive transport model in a porous media (Socié et al. , 2021).

Acknowledgements

The authors would like to thank Alexandre Dauzères and Sidi Souvi for the help in the chemical modeling. We thank the two anonymous reviewers for their constructive critics, suggestions and comments.

Disclosure statement

The authors declare that they have no conflict of interest.

References

M. Al Schamaa, S. Lavaud, L. Divet, J.B. Colliat, G. Nahas, J.M. Torrenti. (2016). Influence of limestone filler and of the size of the aggregates on DEF. Cem. Conc. Compos., 71 175-180.

B. Barbarulo. (2002). Comportement des Matériaux Cimentaires : actions des sulfates et de la température. PhD thesis, Ecole Normale Supérieure de Cachan - Université de Laval

B. Bary. Simplified coupled chemo-mechanical modeling of cement pastes behavior subjected to combined leaching and external sulfate attack. (2008). Int J Numer Anal Meth Geomech, 32, pp. 1791–1816.

B. Bary, A. Lassin, N. Leterrier, E. Deville, P. Le Bescop. (2014). Coupled chemo-transport-mechanical modelling and numerical simulation of external sulfate attack in mortars. Cem. Conc. Compos. 19, pp. 70–83.

L. Bichet. Mécanisme de transport dans la fissuration des matériaux hétérogenes : application a la durée de vie d'éxploitation des centrales nucléaires. (2017). PhD thesis, Université de Montpellier II

M. Bisoffi-Sauve, S. Morel, F. Dubois Modelling mixed mode fracture of mortar joints in masonry buildings Eng. Fracture Mech., 182, pp. 316–330.

N. Blal, L. Daridon, Y. Monerie, S. Pagano. Artificial compliance inherent to the intrinsic cohesive zone models: criteria and application to planar meshes. (2012). Int. J. Fract., 178, pp. 71–83.

Ph. Blanc, A. Lassin, P. Piantone, A. Azaroual, N. Jacquemet, A. Fabbri. E.C. Gaucher. (2012). Thermoddem: A geochemical database focused on low temperature water/rock interactions and waste materials. Appl. Geochemistry, 27 (10), pp. 2107–2116

H. Bouzabata, S. Multon, S. Sellier, H. Houari. (2012). Effects of restraint on expansion due to delayed ettringite formation. Cem. Conc. Res., 42, pp. 1024–1031.

M.H. Bradbury, B. Baeyens. Modelling the sorption of Mn(II), Co(II), Ni(II), Zn(II), Cd(II), Eu(III), Am(III), Sn(IV), Th(IV), Np(V) and U(VI) on montmorillonite: Linear free energy relationships and estimates of surface binding constants for some selected heavy metals and actinides. (2005). Geochimica et Cosmochimica Acta. 69 (4), pp. 875–892.

N.N. Bui. Expansion and stresses induced by crystallization in cement-based materials in presence of sulfate. (2016). PhD thesis, Université ParisEst

N. Cefis, C. Comi, P. Piantone, A. Azaroual, N. Jacquemet, A. Fabbri. (2012). Chemo-mechanical modelling of the external sulfate attack in concrete. Cem. Conc. Res., 93, pp. 57–70

O. Coussy. Poromechanics. (2004). J. Wiley & Sons, Chichester

D. Damidot, F.P. Glasser. Thermodynamic investigation of the $CaOAl_2O_3 - CaSO_4 - H_2O$ system at 50 $°C$ and 85 $°C$. (1992). Cem. Conc. Res., 22, pp. 1179–1191.

C. De Dieuleveult, J. Erhel, M. Kern. A global strategy for solving reactive transport equations. (2009). J. Comput. Phys., (228), pp. 6395–6410

L. Divet, R. Randriambololona. Delayed ettringite formation : the effect of temperature and basicity on the interaction of sulphate and C-S-H phase. (1998). Cem. Conc. Res., 28, pp. 357–363

L. Eddy, A. Awasthi, K. Matsumoto, K. Nagai, S. Asamoto. Mesoscopic analysis of different expansion causes in concrete by 3D Rigid Body Spring Model. (2017). Seisan Kenkyu, (269), pp. 181–185

R. El Hachem, E. Rozière, F. Grondin, A. Loukili. Multi-criteria analysis of the mechanism of degradation of Portland cement based mortars exposed to external sulphate attack. (2012). Cem. Conc. Res., 42, pp. 1327–1335.

R. El Hachem, E. Rozière, F. Grondin, A. Loukili. New procedure to investigate external sulphate attack on cementitious materials. (2012). Cem. Conc. Compos., 34 (3), pp. 357–364.

J. Erhel, T. Migot. Characterizations of solutions in geochemistry: existence, uniqueness, and precipitation diagram. (2019). Comput. Geosci., 23, pp. 523–535

R.J. Flatt, G.W. Scherer. Thermodynamics of crystallization stresses in DEF. (2008). Cem. Conc. Res., 38, pp. 325–336.

E.J. Garboczi, D.-P. Bentz. Analytical formulas for interfacial transition zone properties. (1997). Cem. Based Mat., 6, pp. 99–108.

A.B. Giorla, K.L. Scrivener, C. Dunant. Influence of visco-elasticity on the stress development induced by alkali-silica reaction. (2015). Cem. Conc. Res., 70, pp. 1–8.

Y. Gu. Experimental pore scale analysis and mechanical modeling of cement-based materials submitted to delayed ettringite formation and external sulfate attacks. (2018). PhD thesis, Université Paris-Est.

Y. Gu, R.-P. Martin, O.O. Metalssi, T. Fen-Chong, and P. Dangla. Pore size analyses of cement paste exposed to external sulfate attack and delayed ettringite formation. (2019). Cem. Conc. Res. 123, 105766.

Y. Gu, P. Dangla., R.-P. Martin, O.O. Metalssi, and T. Fen-Chong
Modeling the sulfate attack induced expansion of cementitious materials based on interface-controlled crystal growth mechanisms (2022). Cem. Conc. Res. 152, 106676.

J. Haas, A. Nonat. From csh to cash: Experimental study and thermodynamic modelling.(2015). Cem. Conc. Res., 68, pp. 124–138.

C.-J. Haecker, E.J. Garboczi, J.W. Bullard, R.B. Bohn, Z. Sun, S.P. Shah, T. Voigt. Modeling the linear elastic properties of Portland cement paste. (2005). Cem. Conc. Res., 35, pp. 1948–1960.

Z. Hashin, P.J.M. Monteiro. An inverse method to determine the elastic properties of the interphase between the aggregate and the cement paste. (2002). Cem. Conc. Res., 32, pp. 1291–1300.

Honorio, T. AND Bary, B. AND Benboudjema, F. Multiscale estimation of ageing viscoelastic properties of cement-based materials: A combined analytical and numerical approach to estimate the behaviour at early age. (2016). Cem. Conc. Res., 87, pp. 137–155.

A.E Idiart, J. Bisschop, A. Caballero, P. Lura. A numerical and experimental study of aggregate-induced shinkrage craking in cementitious composites. (2012). Cem. Conc. Res., 42, pp. 272–281.

A.E Idiart, C.M. López, I. Carol. Chemo-mechanical analysis of concrete cracking and degradation due to external sulfate attack: A meso-scale model. (2011). Cem. Conc. Compos., 33, 411–423.

A.E Idiart, M. Laviña, B. Cochepin, A. Pasteau. (2020). Hydro-chemo-mechanical modelling of long-term evolution of bentonite swelling. App. Clay. Sc., 195, doi.org/10.1016/j.clay.2020.105717

L. Irbe, R.E Beddoe, D. Heinz. The role of aluminium in C A S H during sulfate attack on concrete. (2019). Cem. Conc. Res., 116, pp. 71–80.

J. Jabbour. Méthodes d'essais de vieillissement accéléré des bétons á l'échelle des ouvrages. (2018). PhD thesis, Université ParisSaclay

S. Kamali-Bernard, F. Bernard, W. Prince. Computer modelling of tritiated water diffusion test for cement based materials. (2009). Comput. Mat. Sci., 45, pp. 528–535.

M.M. Karthik, J.B. Mander, S. Hurlebaus. ASR/DEF related expansion in structural concrete: Model development and validation. (2016). Constr. Build. Mat.,128, pp. 238–247.

B. Kchakech. Etude de l'influence de l'échauffement subi par un béton sur le risque d'expansions associées à la Réaction Sulfatique Interne. (2016). PhD thesis, Université Paris-Est.

T. Kadeethum, S. Lee, F. Ballarin, J. Choo, H.M. Nick A locally conservative mixed finite element framework for coupled hydro-mechanical–chemical processes in heterogeneous porous media (2021). Comput. Geosci.,152, pp. 104774, `https://www.sciencedirect.com/science/article/pii/S0098300421000790`.

W. Kunther, B. Lothenbach, K. L. Scrivener On the relevance of volume increase for the length changes of mortar bars in sulfate solutions (2013). Cem. Conc. Res., 46, pp 23–29.

V. Lagneau, J. van der Lee. Hytec results of the momas reactive transport benchmark. (2010). Comput. Geosci., 14, pp. 435–449

A.N. Leklou, J.E. Aubert, G. Escadeillas. Effect of wetting-drying cycles on mortar samples affected by DEF. (2012). Eur. J. Environ. Civ. Eng., 16, pp. 582–588.

E. Lemarchand, L. Dormieux, F.-J. Ulm. Elements of micromechanics of ASR-induced swelling in concrete structures. (2002). Conc. Sci. Eng., 4, pp. 12–22.

J. Liaudat, I. Carol, C.M. López. Model for alkali-silica reaction expansions in concrete using zero-thickness chemo-mechanical interface elements. (2020). Int. J. Solids Struc., 207, pp. 145–177.

J., Lhonneur. Approche par changement d'échelle du vieillissement des bétons : expérimentations et simulations numériques. (2021). PhD thesis, Université de Montpellier

B. Lothenbach, D. Kulik, T. Matschei, M. Balonis, L. Baquerizo, B.Z. Dilnesa. D.G. Miron, R. Myers, Cemdata18: A chemical thermodynamic database for hydrated portland cements and alkali-activated materials. (2019). Cem. Conc. Res., 115 , pp. 472–506

M. Malbois, B. Nedjar, S. Lavaud, C. Rospar, L. Divet, J.M. Torrenti. On DEF expansion modelling in concrete structures under variable hydric conditions. (2019). Constr. Build. Mater., 207, pp. 396–402.

C. Marquié, A. Dauzeres, B. Richard, G. Nahas. Concrete aging in containment building and deep geological disposal facilities: the ODOBA project. (2019). Proceeding Transactions, SMiRT-25 Charlotte, NC, USA

R.-P. Martin, O.O. Metalssi, F. Toutlemonde. Importance of considering the coupling between transfer properties, alkali leaching and expansion in the modelling of concrete beams affected by internal swelling reactions. (2013). Constr. Build. Mater., 49, pp. 23–30.

T. Miura,I. Maruyama, H. Nakamura, Y. Yammoto. Feedback System of Ion Transfer through Cracks During Deterioration of Mortar Due to Sulfate Attack Evaluated by RBSM-Truss Network Model. (2017). J. Adv. Conc. Tech0., 15 (10), pp. 610–626

T. Miura, H. Nakamura, Y. Yammoto. Impact of origination of expansion on three-dimensional expansion crack propagation process due to DEF evaluated by mesoscale discrete model. (2020). Constr. Build. Mater. 260, 119911.

Y. Monerie, V. Acary. Formulation dynamique d'un modèle de zone cohésive tridimensionnel couplant endommagement et frottements. (2001). Revue européenne des éléments finis, 10, pp.

489–503.

F. Morel, J. Morgan. A numerical method for computing equilibria in aqueous chemical systems. (1972). Environ. Sci. Tech., 6 (1), pp. 58–67

P. Morenon, S. Multon, A. Sellier,E. Grimal, F. Hamon, E. Bourdarot. Impact of stresses and restraints on ASR expansion. (2017). Constr. Build. Mater.,140, pp. 58–74.

T. Mori, K. Tanaka. Average stress in matrix and average elastic energy of materials with misfitting inclusions. (1957). Acta Metallurgica., 21 (5), pp. 571–574

S. Multon.A. Sellier. Expansion modelling based on cracking induced by the formation of new phases in concrete. (2019). Int. J. Solids Struc., 160, pp. 293–306.

M. Neji, B. Bary, P. Le Bescop, N. Burlion. Swelling behavior of ion exchange resins incorporated in tri-calcium silicate cement matrix: I. chemical analysis. (2015). J. Nucl. Mater., 467, pp. 544–556

R.A. Patel, Q.T. Phung, S.C. Seetharam, J. Perko, D. Jacque, N. Maes, G. De Schutter, G. Ye, K. Van Breugel. Swelling behavior of ion exchange resins incorporated in tri-calcium silicate cement matrix: I. chemical analysis. (2016). Cem. Conc. Res., 90, pp. 52–72

F. Perales, S. Bourgeois, A. Chrysochoos, Y. Monerie. Two field multibody method for periodic homogenization in fracture mechanics of non linear heterogeneous materials. (2008). Eng. Fracture Mech., 75, pp. 3378–3398.

F. Perales, F. Dubois, Y. Monerie, B. Piar, L. Stainier. A NonSmooth Contact Dynamics-based multi-domain solver. Code coupling (Xper) and application to fracture. (2010). Eu. J. Comput. Mech., 19, pp. 389–417.

D. Planel. Les effets couplés de la précipitation d'espèces secondaires sur le comportement mécanique et la dégradation chimique des bétons. (2002). PhD thesis, Université de Marne la Vallée.

D. Planel, J. Sercombe, P. Le Bescop, F. Adenot, J.M. Torrenti. Long-term performance of cement paste during combined calcium leaching-suflate attack: kinetics and size effect. (2006). Cem. Conc. Res., 36, pp. 137–143.

S. Qin, D. Zou, T. Liu, A. Jivkov. A chemo-transport-damage model for concrete under external sulfate attack. (2020). Cem. Conc. Res., 132, 106048.

N.Salah, J. Mouad, E. Malachanne, F. Jamin, F. Dubois, A.S. Caro, E. GarciaDiaz, M.S. El Youssoufi. Identification of a cohesive zone model for cement paste-aggregate interface in a shear test. (2019). Eur. J. Environ. Civ. Eng., pp. 1–15, DOI: `https://doi.org/10.1080/19648189.2019.1623082`.

E. Samson, J. Marchand. Modeling the transport of ions in unsaturated cement-based materials. (2007). Computers Struct., 85, pp. 1740–1756

M. Salgues, A. Sellier, S. Multon, E. Bourdarot, E. Grimal. DEF modelling based on thermodynamic equilibria and ionic transfers for structural analysis. (2014). Eur. J. Environ. Civ. Eng. 18 (4), pp. 1–26.

N. Seigneur, V.Lagneau, J. Corvisier, A. Dauzéres Recoupling flow and chemistry in variably saturated reactive transport modelling - An algorithm to accurately couple the feedback of chemistry on water consumption, variable porosity and flow. (2018). Adv. Wat. Res., 122, pp. 355–366.

A. Sellier, S. Multon. Chemical modelling of delayed ettringite formation for assessment of affected concrete structures. (2018). Cem. Conc. Res., 108, pp. 72–86.

A. Socié, Modélisation chimiomécanique de la fissuration de matériaux cimentaires : vieillissement et tenue des enceintes de confinement des centrales nucléaires. (2019). PhD thesis, Université de Montpellier

A. Socié, F. Dubois., Y. Monerie, F. Perales. Multibody approach for reactive transport modeling in discontinuous-heterogeneous porous media. Comput. Geosci., 25 (5), pp. 1473–1491, DOI: `https://doi.org/10.1007/s10596-021-10058-x`.

A. Socié, Y. Monerie, F. Perales. Effects of the microstructural uncertainties on the poroelastic and the diffusive properties of mortar. J. Th. Comput. Appl. Mech., DOI: `https://doi.org/10.46298/jtcam.8849`.

A. Soive, E. Roziere, A. Loukili. Parametrical study of the cementitous materials degradation under external sulfate attack through numerical modeling. (2016). Constr. Build. Mat., 112, pp. 267–275.

A. Soive, V.Q. Tran. External sulfate attack of cementitious materials: New insights gained through numerical modeling including dissolution/precipitation kinetics and surface complexation. (2017). Cem. Conc. Compos., 83, pp. 263–272.

C.I. Steefel, C.A.J. Appelo, B. Arora, D. Jacques, T. Kalbacher, O. Kolditz, V. Lagneau, P.C. Lichtner, K.U. Mayer, J.C.L. Meeusen, S. Molins, D. Moulton, H. Shao, J. Simůnek, N. Spycher, S.B. Yabusaki, G.T. Yeh. Reactive transport codes for subsurface environmental simulation. (2015). Comput. Geosci., 19, pp. 445–478.

C.I. Steefel Reactive Transport at the Crossroads. (2019). Reviews in Mineralogy and Geochemistry, 85 (1), pp. 1–26, doi:`https://doi.org/10.2138/rmg.2019.85.1`.

E. Stora, B. Bary, Q.-C. He, E. Deville, P. Montarnal. Modelling and simulations of the chemo-mechanical behaviour of leached cement-based materials leaching process and induced loss of stiffness. (2009). Cem. Conc. Res., 39, pp. 763–772

P.D. Tennis, H.M. Jenning. Model for the Developing Microstructure in Portland Cement Pastes. (1994). J. Am. Ceram. Soc., 77, pp. 3161–3172

R. Tixier, B. Mobasher. Modeling of damage in cement-based materials subjected to external sulfate attack. I: Formulation. II: Comparison with experiments. (2003). ASCE J. Mat. Civil Engng., 15, pp. 305–322

J.-F. Ulm, B. Constantinides, F.H. Heukamp. Is concrete a poromechanics material? -A multiscale investigation of poroelastic properties. (2004). Mat. Struct. Conc. Sci. Eng., 37, pp. 43–58

J. van Der Lee, L. De Windt, V. Lagneau, Goblet, P. Module-oriented modeling of reactive transport with HYTEC. (2003). Comput. Geosci., 29 (3), pp. 265-275

V. Venzal, S. Morel, T. Parent, F. Dubois. Frictional cohesive zone model for quasi-brittle fracture: Mixed-mode and coupling between cohesive and frictional behaviors. (2020). Int. J. Solids Struc., 198, pp. 17–30

Appendix A. Estimation of the initials properties

The application focuses on the chemo-mechanical behavior of a cement paste and mortar. As usually considered, the mortar microstructure is decomposed into two elementary levels (Socié et al. , 2022) (Figure A1):

(1) cement paste : composed of C-S-H matrix, hydrate inclusions and capillarity pores. We consider the main hydrates: portlandite, ettringite and katoite.
(2) mortar : composed of cement paste matrix, the interfacial transition zone (ITZ) and sand particles.

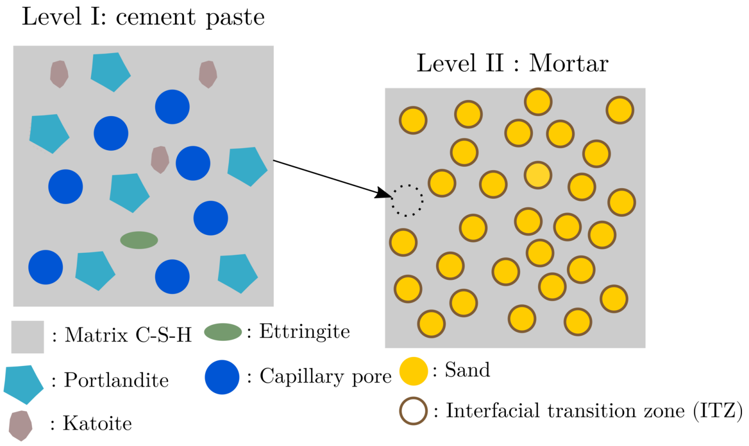

Figure A1. Schematic of the multi-scale representation used for the estimation of the material properties.

The initial properties are computed into two steps: estimation of the microstructure through a hydration computation, and evaluation of the diffusive and poro-elastic parameters by analytical homogenization.

A.1. Estimation of the microstructure

The cement paste microstructure is estimated by a static chemical computation model based on the assumption of a totally hydrated reaction (Socié , 2019). With the mass fraction of each components of the clinker, noted f_i^m for the solid i, the water cement mass ratio w/c, the total concentration of each main component are estimated [$mol.L^{-1}$ porous medium]:

$$\begin{cases} (C_{tot}^{aq})_{Ca^{2+}} = 3C_{C_3S} + 2C_{C_2S} + 3C_{C_3A} + C_{CaSO_4} + 4C_{C_4AF} \\ (C_{tot}^{aq})_{H_2SiO_4^{2-}} = C_{C_3S} + C_{C_2S} \\ (C_{tot}^{aq})_{SO_4^{2-}} = C_{CaSO_4} \\ (C_{tot}^{aq})_{Al(OH)_4^-} = 2C_{C_3A} + 2C_{C_4AF} \end{cases} \tag{A1}$$

with (Planel , 2002):

$$m_{ci} = \frac{V_{total}\rho_{ci}}{\frac{w}{c}\frac{\rho_{ci}}{\rho_w} + 1}; \quad (C_{tot}^{aq})_i = \frac{M_i f_i^m m_{ci}}{V_{total}} \quad \forall i \in [1, 4] \tag{A2}$$

with i is the species, M_i is the molar mass [$kg.mol^{-1}$], m_{ci} is the cement mass [m], ρ_{ci} is the cement density [$kg.m^{-3}$], ρ_w is the water density [$kg.m^{-3}$] and V_{total} is the total volume [m^3].

The hydration model considers the precipitation of the main hydrate of the cement paste and gives the concentration of each component. The chemical reactions, the aqueous components and the equilibrium constant are described in the Table 1 and A1.

Chemical equation	$\log_{10}(K^{sol})$
$C-S-H(1.65) + 2H_2O \Longleftrightarrow 1.65Ca^{2+} + 3.3OH^- + SiO_2$	-17.64

Table A1. Chemical reaction for the hydration simulation (Blanc et al. , 2012; Lothenbach et al. , 2019).

Estimation of the porosity: The cement paste porosity, ϕ_{cp}, is obtained from the hydration product:

$$\phi_{cp} = 1. - \sum_{i=1}^{N^{sol}} V_i (C_i^{sol})^* = 1. - \sum_{i=1}^{N^{sol}} \varphi_i \tag{A3}$$

where $(C_i^{sol})^*$ is the solid concentration in $mol.L^{-1}$ of cement paste, obtained by the chemical computation.

The total porosity is computed by the molar volume of dried C-S-H and in that way, the porosity contains the gel and the capillary porosity. To apply the micromechanical model, we need to distinguish the capillarity porosity from the total cement paste porosity. Based on the work of Tennis & Jenning (1994):

$$\phi_{cp} = \phi_{csh} + \phi_{cap} \quad \text{with: } \phi_{csh} = \alpha_{csh}(\varphi_{csh})^{\diamond} \tag{A4}$$

where $(\varphi_{csh})^{\diamond}$ is the volume fraction of wet C-S-H (dried C-S-H and saturated gel porosity), and α_{csh} is a function parameter that we consider equal to 0.28 (Tennis & Jenning , 1994).

To apply a micromechanical scheme at the cement paste scale, the following restriction must be satisfied:

$$\phi_{cap} = 1. - \sum_{i=1}^{N^{sol}-1} V_i (C_i^{sol})^* - (\varphi_{csh})^\diamond \tag{A5}$$

We deduce the following result:

$$(\varphi_{csh})^\diamond = \frac{\varphi_{csh}}{1 - \alpha_{csh}} \quad \phi_{cap} = \phi_{cp} - \frac{\alpha_{csh}\varphi_{csh}}{1 - \alpha_{csh}} \tag{A6}$$

At the mortar scale, the porosity is a function of the capillary and ITZ porosity. In the first approximation, we consider the ITZ porosity as a function of the cement paste value (Socié et al. , 2022). We deduce the mortar porosity, ϕ_m:

$$\phi_m = \varphi_{itz}\phi_{itz} + \varphi_{cp}\phi_{cp} = (\varphi_{itz}\alpha_{itz} + \varphi_{cp})\,\phi_{cp} \tag{A7}$$

φ_{itz} and φ_{cp} define the volume fraction of ITZ and cement paste respectively. α_{itz} is a parameter that admits a value between 1.5 and 4 in the literature (Socié et al. , 2022). We consider $\alpha_{itz} = 2$.

In the reactive transport model, the solid concentration are expressed in $mol.L^{-1}$ of solution (6) and their volume fraction (volume solid/volume of porous medium) must satisfy the equations (9) and (10). For the cement paste, the solid concentration are obtained directly from the hydration product:

$$C_i^{sol} = \frac{(C_i^{sol})^*}{\phi_{cp}} \tag{A8}$$

At mortar scale, the solid volume fraction (L/L of mortar) and the concentration (mol/L of solution) are related to the total porosity by the following equations :

$$\phi_m = 1 - \sum_{i}^{N^{sol}} \varphi_i^{mt} - \varphi_s = (\varphi_{itz}\alpha_{itz} + \varphi_{cp})\,\phi_{cp}; \quad \varphi_i^{mt} = \phi V_i C_i^{sol} \tag{A9}$$

where φ_s is the sand volume fraction and φ_i^{mt} is the solid volume fraction at mortar scale. There is not a direct link between the volume fraction of solid at cement paste scale, denoted φ_i^{cp}, and at mortar scale, because hydrates compose also a part of the ITZ phase (Honorio et al. , 2016). We consider the same repartition coefficient, denoted r, for all the hydrates between the ITZ and the cement paste. We thus deduce:

$$\phi_m = 1 - \sum_{i}^{N^{sol}} \varphi_i^{mt} - \varphi_s = 1 - \sum_{i}^{N^{sol}} \varphi_i^{cp} r - \varphi_s \quad \Rightarrow \quad r = \frac{1 - \phi_m - \varphi_s}{1 - \phi_{cp}} \tag{A10}$$

We then deduce the solid fraction at mortar scale and the solid concentration for the mortar simulation:

$$\varphi_i^{mt} = r V_i (C_i^{sol})^*; \quad C_i^{sol} = \frac{r (C_i^{sol})^*}{\phi_m} \quad \forall i \in [1, N^{sol}] \tag{A11}$$

A.2. Effective poro-elastic and diffusive properties at mortar scale

Knowing the microstructure, the material properties are deduced by analytical homogenization. We assumed a spheric inclusion distribution in a isotropic material. The retained homogenization schemes follow recommendations of the literature (Socié et al. , 2022):

- Cement paste: Mori-Tanaka's scheme (Mori & Tanaka , 1973), also used in (Bary , 2008; Ulm et al. , 2004).
- Mortar: Generalized Self-Consistent scheme (Hashin & Monteiro , 2002), also used in (Bary et al. , 2014; Stora et al. , 2009).

The sand phase is considered as a no reactive and no diffusive phase with an elastic mechanical behavior. We choose to not represent explicitly the ITZ phase due to the great uncertainty of the material parameters (Patel et al. , 2016; Socié , 2019; Socié et al. , 2022), and we consider the ITZ properties are a function of the cement paste parameters.

Finally, we consider the ettringite precipitate only in the capillary and ITZ pore, and thus we do not consider the C-S-H Biot coefficient. Moreover, the model can estimate the impact of the ettringite concentration behavior on the overall swelling. The main material properties are sum up in the Table A2. For more details on the homogenization model and the overall equations, see (Socié et al. , 2022).

	D_i $[m^2.s^{-1}]$	k_i $[GPa]$	g_i $[GPa]$	V_i $[L.mol^{-1}]$	References
C-S-H	4.64×10^{-12}	14.9	9	0.084	(Haecker et al. , 2005) (Planel , 2002) (Socié et al. , 2022)
Portlandite	0	40	16	0.033	(Haecker et al. , 2005) (Lothenbach et al. , 2019)
Ettringite	0	14.9	9	0.707	(Haecker et al. , 2005) (Lothenbach et al. , 2019)
Katoite	0	14.9	9	0.15	(Haecker et al. , 2005) (Lothenbach et al. , 2019)
Capillary pore	2×10^{-9}	0	0	0	(Bary , 2008)
ITZ	$4 \times D_{pdc}$	$k_{pdc}/2$	$g_{pdc}/2$	0	(Hashin & Monteiro , 2002) (Kamali-Bernard et al. , 2009)
Sand	0.	35.9	25.8	0	(Stora et al. , 2009)

Table A2. Diffusivity coefficient D_i, bulk modulus k_i, shear modulus g_i, and molar fraction V_i of the main phases. The subscript *pdc* define the cement paste properties.